Elimination of senescent cells with senolytic host-directed therapy reduces tuberculosis progression in mice

List of authors.

Somnath Shee[1], Yazmin B. Martinez-Martinez[1], Benjamin Koleske[1], Shivraj Yabaji[2], Lester Kobzik[3], Igor Kramnik[2], William Bishai[1,#]

[1] Center for Tuberculosis Research, Johns Hopkins University, School of Medicine, Baltimore, MD, USA.

[2] The National Emerging Infectious Diseases Laboratories (NEIDL), Boston University, Boston, MA, USA.

[3] Cellecta, Inc, Mountain View, CA, USA

[#] For correspondence: wbishai1@jhmi.edu (William Bishai)

Short title: Senolytic therapy for TB

Keywords.

Senescence, Aging, Tuberculosis, Mycobacterium, Senolytics, Dasatinib, Quercetin, Fisetin, Granuloma, Necrosis, SASP, DNA damage

Graphical abstract

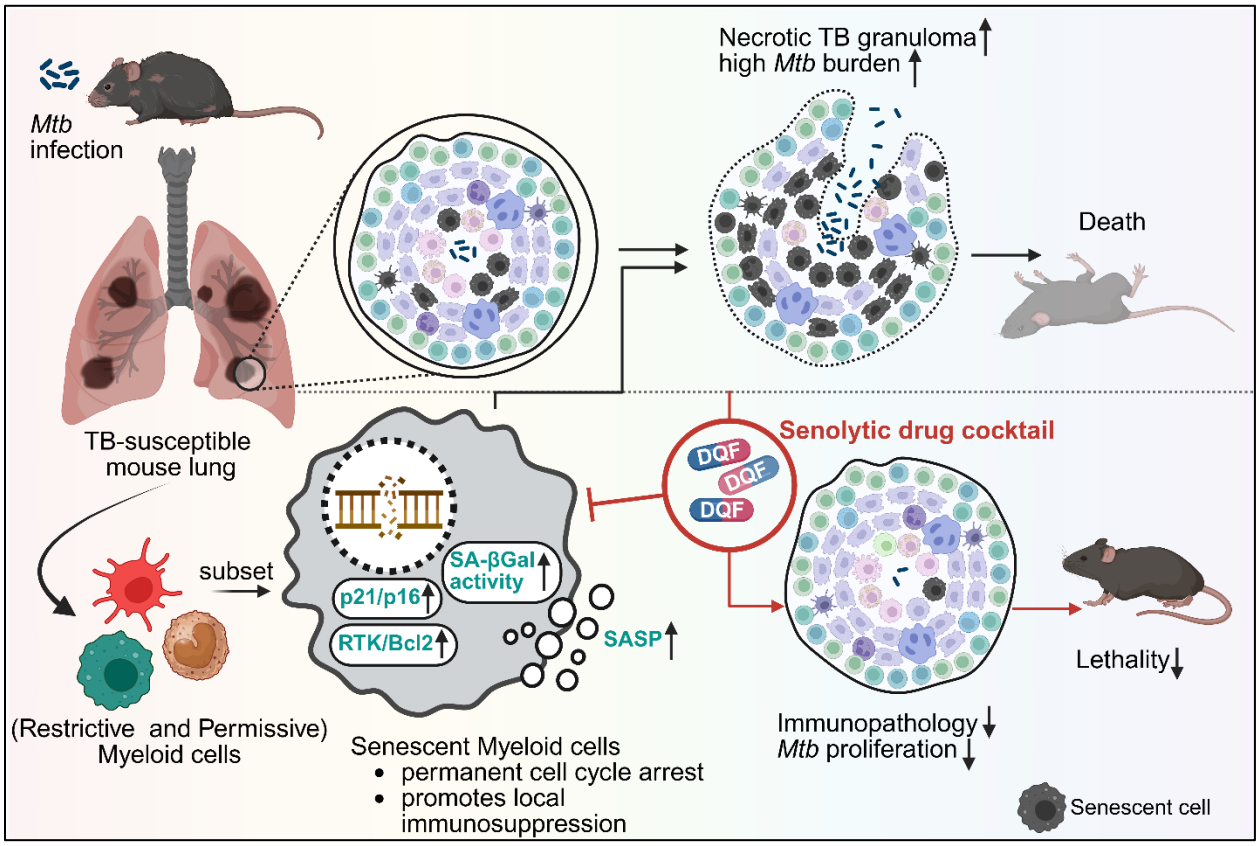

Highlights

- *Mtb* lung infection results in recruitment of both restrictive and permissive myeloid cells to the nascent granuloma.
- *Mtb* infection induces certain permissive myeloid cells to enter a senescent state, characterized by cell cycle arrest and they promote local immunosuppression.
- Treatment with a Senolytic drug cocktail, which kills senescent cells, augments host resistance against *Mtb* proliferation, lethality and immunopathology.

Summary/ Abstract

By eliciting lung necrosis, which enhances aerosol transmission, *Mycobacterium tuberculosis* (*Mtb*) sustains its long-term survival as a human pathogen. In studying the human-like necrotic granuloma lesions characteristic of *Mtb*-infected *B6.Sst1S* mice, we found that lung myeloid cells display elevated senescence markers: cell cycle arrest proteins p21 and p16, the DNA damage marker γH2A.X, senescence-associated β-galactosidase activity, and senescence-associated secretory phenotype (SASP). These markers were also elevated in *Mtb*-infected aged wild type (WT) mice but not in young WT mice. Global transcriptomics data revealed upregulation of pro-survival (PI3K, MAPK) and anti-apoptotic pathways in *Mtb*-infected *B6.Sst1S* macrophages. As senescent cells are terminally growth-arrested yet metabolically active cells that release tissue-damaging, immunosuppressive SASP, we treated *Mtb*-infected mice with a cocktail of three senolytic drugs (dasatinib, quercetin, and fisetin) designed to kill senescent cells. Senolytic drug treatment prolonged survival and reduced *Mtb* lung counts in *B6.Sst1S* and aged WT mice to a greater degree than young WT mice and concomitantly reduced lung senescence markers. These findings indicate that (1) *Mtb* infection may induce lung myeloid cells to enter a senescent state and that these cells may promote disease progression, and (2) senolytic drugs merit consideration for human clinical trials against tuberculosis (TB).

54 **Introduction**

55 Despite the introduction of 3 new anti-tuberculosis (TB) drugs since 2012, the global TB
56 pandemic remains poorly controlled.[1] Most humans are resistant to TB and are capable
57 of limiting the bacterial growth and inflammatory damage caused by *Mycobacterium*
58 *tuberculosis* (*Mtb*) infection.[2–4] However, susceptible individuals develop active disease
59 characterized by necrotic granulomatous lung lesions that may further transform into lung
60 cavities, leading to lung damage and morbidity even with appropriate anti-TB treatment,
61 and ultimately TB transmission.[5,6] Understanding the molecular basis for failed granuloma
62 control and necrotic lesion formation is a major unmet need in TB research.

63 While it is well known that aging is a significant risk factor for progression from contained
64 *Mtb* infection to active TB disease in both high and low-level income countries,[7–11] there
65 have been relatively few studies investigating the mechanistic basis for age-associated
66 active TB.[12–20] Senescence is a rapidly expanding research discipline as many
67 investigators have sought to understand the mechanism of gradual tissue failure in age-
68 associated chronic diseases such as dementia, heart failure, arthritis, and renal failure.[21]
69 The accumulation of senescent cells is a principal mechanism of functional tissue
70 impairment in aging.[22,23] A key lesson from the senescence literature is that aged tissues
71 are populated by long-lived, non-dividing, functionally impaired senescent cells. These
72 cells release deleterious signaling molecules- collectively termed senescence-
73 associated secretory phenotype (SASP), that locally contribute to immunosuppression,
74 dysregulated inflammation, and tissue failure.[24–27] Indeed, transplantation of isolated
75 senescent cells led to premature aging in mice.[28,29] In this context, small molecule
76 senolytic drugs—designed to induce apoptosis in the non-dividing senescent cells—

77 prolong murine lifespan, and improve organ function in humans with chronic disease.[30,31]
78 To gain insight into the factors that lead to the loss of immune containment of *Mtb*, we
79 study the *B6.Sst1S* mice, which develop human-like necrotic lung granulomas following
80 *Mtb* infection in contrast to most wild type (WT) mouse strains.[32–38] These mice harbor
81 the *Sst1S* allele, which has loss of function mutations in the Sp140 chromatin remodeling
82 protein that plays a key role in immune cell gene regulation.[39,40] Additionally, the closely
83 related *Sp140*$^{-/-}$ mouse strain was characterized to exhibit a population of interstitial
84 macrophages (IM) and plasmacytoid dendritic cells (pDC) that aberrantly secrete type I
85 IFN (associated with TB exacerbation),[41–43] are poorly responsive to IFNγ, and may play
86 a key role in granuloma breakdown in these mice.[44]

87 In this paper, we report that a distinct population of lung myeloid cells in *Mtb*-infected
88 *B6.Sst1S* mice display higher levels of senescence markers prior to necrotic granuloma
89 formation and are subsequently found in close association with non-controlling, early
90 necrotic granulomas. Similar senescence marker increases are present in aged, *Mtb*-
91 infected WT C57BL/6 (B6) mice, but not young WT B6 mice. Treatment with a three-drug
92 cocktail of FDA-approved senolytic drugs to eliminate these senescent cells restored
93 containment of *Mtb* proliferation, prolonged mouse survival, and reduced
94 immunopathology and senescence markers. Thus, during TB infection a population of
95 lung myeloid cells enters a senescent state and may contribute to failure of immune
96 containment and progression to necrosis.

97

98

Results

Elevated senescence markers were detected in BMDMs from *B6.Sst1S* and aged WT B6 but not young WT B6 mice *in vitro*.

We previously observed that TNFα exposure induced a stress response characterized by overexpression of IFNβ (Figure S1A) and the integrated stress response (ISR) in *B6.Sst1S* bone marrow-derived macrophages (BMDMs).[37,38] Reanalysis of transcriptomic signatures in uninfected *B6.Sst1S* versus WT B6 BMDMs with and without TNFα treatment (GSE99456)[38] suggested upregulation of cellular senescence pathways, enhanced DNA damage responses, activation of mitotic checkpoints, pro-survival ERK1/ERK2 protein kinase cascade, and cellular response to IFNβ (by Metascape Analysis;[45] Figure S1B-S1D, Supplementary File S1) in *B6.Sst1S* BMDMs. Because chronic ISR activation and heightened Type I interferon exposure can be a potential trigger of cellular senescence,[46–50] we tested uninfected TNFα-stimulated BMDMs from young *B6.Sst1S* mice (8-12 weeks old) alongside BMDMs from young and aged (>72 weeks old) WT B6 mice for the presence of canonical senescence markers (Figure 1A).[51–54] *B6.Sst1S* and aged WT B6 BMDMs showed greater activity of senescence-associated β-galactosidase (SA-βGal) than young WT B6 BMDMs, although not to the level seen with etoposide, an inducer of DNA damage-mediated senescence (Figure 1B- 1D, Figure S2A). In addition, we observed the induction of SASP genes (*Il1β, Il1α, Il6, Mmp12, Mmp13, Ccl2, Ccl8, Pai1*) transcription in TNFα-treated *B6.Sst1S* BMDMs compared to similarly treated WT B6 cells (Figure 1E). Moreover, TNFα- treated *B6.Sst1S* BMDMs and aged WT B6 BMDMs showed the presence of established biomarkers of senescence: higher levels of the cyclin-dependent kinase inhibitor P16 (cell cycle arrest), higher

122 phospho(S139)-H2A.X (DNA damage marker), lower Lamin B1 (structural constituent of
123 the nuclear lamina, Figure S2B), and reduced cell proliferation as measured by BrdU-
124 incorporation assay (Figure 1F, S2C) without a significant reduction in viability (Figure
125 S2D). BMDMs from young *B6.Sst1S* and aged WT B6 mice (the same cells with higher
126 senescence markers following TNFα induction) showed poorer *Mtb* containment than
127 those from young WT B6 (Figure 1G). In sum, in line with the transcriptomics data, TNFα-
128 treated *B6.Sst1S* BMDMs indeed exhibited numerous markers of senescence similar to
129 BMDMs from aged WT B6 mice or etoposide-treated WT B6 controls.

130 **Senescence markers are elevated in non-controlling lung lesions of *B6.Sst1S* mice**
131 **and in lung myeloid cells from *Mtb*-infected young *B6.Sst1S* and aged WT B6 mice.**

132 To examine whether senescence signatures appear in the context of active lung infection,
133 we performed spatial transcriptomics to profile neighboring cells associated with
134 controlling (C) versus non-controlling (NC) lesions in *B6.Sst1S* mouse lungs (Figure 2A).
135 To do this, we first administered $1x10^6$ CFU of *Mtb* subcutaneously in the hock of
136 *B6.Sst1S* mice and allowed generation of chronic lesions in a post-primary pulmonary TB
137 model.[55] Lung samples were harvested at 14 weeks post-infection and subjected to
138 unbiased spatial transcriptomics targeting cells near lesions. We categorized the lesions
139 into non-controlling (NC; advanced multibacillary lesions with necrotic cores) and
140 controlling granulomas (C; non-necrotic paucibacillary lesions), as determined by acid-
141 fast and H&E staining (Figure 2A). We identified 734 differentially expressed genes
142 (DEGs; $\log_2$fold change>1 or <-1, adjusted $p< 0.05$) in the neighboring cells from NC vs
143 C lesions (Figure 2B, Supplementary File S2). Functional pathway enrichment analysis[45]
144 identified inflammatory response, extracellular matrix organization, lung fibrosis and

145 negative regulation of cell proliferation pathways to be significantly higher in NC lesions
146 (Figure S3A). Moreover, there was a statistically significant overlap between NC vs C
147 lesion- DEGs and the SenMayo[56] senescence-associated gene set (Fisher's exact test,
148 two-sided, $p < 0.0001$; Figure S3B, S3C) indicating enrichment of senescence-associated
149 genes in non-controlling lung lesions. These spatial transcriptomics data indicate that lung
150 cells expressing senescence markers are uniquely present near and within granulomas
151 progressing to necrosis in *Mtb*-infected *B6.Sst1S* mouse lungs.

152 To examine the accumulation of senescence markers *in vivo*, we infected young
153 *B6.Sst1S*, young WT B6 mice, and aged WT B6 mice with *Mtb* by the aerosol route
154 (Figure 2C). *Mtb* proliferation was significantly higher uniquely in young *B6.Sst1S* mice,
155 with necrosis appearing as early as 4 weeks post-infection (wpi) (Figure 2D, 2G). Both
156 young *B6.Sst1S* and aged WT B6 showed increased dissemination to the spleen at 6 wpi,
157 suggesting that aged WT B6 mice have a defect in containment compared to young WT
158 B6 (Figure 2E). At 2 wpi, when lung CFU counts were equivalent across all three groups,
159 we observed a higher degree of immunopathology as measured by area of lung
160 consolidation in the H&E-stained lungs of aged WT B6 compared to young WT B6 (p=
161 0.03), while young *B6.Sst1S* mice showed similar degree of lung disease (p=0.48, Figure
162 2F, 2H). At 4 wpi the degree of pathology in aged WT B6 mice lungs remained the same
163 as at 2 wpi, while there was considerable progression in young *B6.Sst1S* and young WT
164 B6 (Figure 2G, 2H).

165 Next, to extend our *in vitro* observations with BMDMs, we aimed to determine if markers
166 of senescence were similarly elevated during *in vivo* mouse infections. We evaluated lung
167 levels of γH2A.X and cyclin-dependent kinase inhibitor p21 by immunohistochemistry at

168 the 2 wpi timepoint, when no differences in CFU and histopathology were present (Figure
169 2D, 2F, 2H). Interestingly, we observed that both young *B6.Sst1S* and aged WT B6 mice
170 showed qualitatively higher immunostaining for γH2A.X and p21 by IHC (Figure 2F), and
171 these levels continued to increase at 4 wpi in *B6.Sst1S* mice but not aged WT B6 (Figure
172 2G). Quantification of the γH2A.X-stained area and γH2A.X staining-intensity of the lung
173 confirmed significantly elevated levels for both *B6.Sst1S* and aged WT B6 mice relative
174 to young WT B6 mice at 2 wpi (Figure 2I, 2J). To refine this analysis, we turned to flow
175 cytometric measurements of widely accepted senescence markers (p21, p16 and SA-
176 βGal)[53,57] with lung and spleen cells (Figure 3A, Figure S4). To examine the temporal
177 relationship (cause or effect) between senescence and elevated *Mtb* burden, we
178 measured the senescent cell populations at an early time point, 10 days post-infection
179 (dpi) when lung CFU burdens are the same across all groups (Figure 3B, 3C, Figure S5A).
180 We found that the percent double positive $p16^{+}p21^{+}$ cells and the percent SA-βGal^{+} cells
181 out of all live cells were significantly higher (≈2-3-fold) in the lungs of *Mtb*-infected young
182 *B6.Sst1S* and aged WT B6 mice than in young WT B6 at 10 dpi (Figure 3D, 3E).
183 Senescence markers in spleen cells were not elevated in any group at this 10 dpi (Figure
184 3D, 3E), likely because there was little or no *Mtb* dissemination to spleen (Figure 3C).
185 Importantly, myeloid cells— predominantly alveolar (AM) and interstitial macrophages
186 (IM) accounted for the majority of the enrichment in senescence markers (double positive
187 $p16^{+}p21^{+}$ cells and SA-βGal^{+} cells) as seen in young *B6.Sst1S* and aged WT B6 mice
188 lung cells (Figure 3F, 3G). No differences in senescence marker abundance between the
189 three types of mice were observed for B cells, and with T cells we found a modest
190 elevation of SA-βGal^{+} senescence marker in aged WT B6 mice which was not seen with

191 the double positive p16^{+}p21^{+} marker (Figure 3F, 3G). Similar data were observed at 20
192 dpi (Figure S5B, S5C). Lastly, we evaluated lung levels of SASP cytokines in mice lungs.
193 We did not detect enrichment of cytokine levels in mouse lungs at 10 dpi, except IL-17a
194 in aged WT B6 (Figure S5D**).** However, five of the eight tested (IL-1β, IL-6, TNFα, IL-17a,
195 and GM-CSF) were significantly elevated in young *B6.Sst1S* mouse lungs compared to
196 young WT B6, although no differences were seen in aged WT B6 at 4 wpi and 20 dpi
197 (Figure 3H). Thus during *in vivo* mouse infections, certain senescence markers—most
198 notably macrophages doubly positive p16^{+}p21^{+}, SA-βGal^{+}, and overall γH2A.X levels--
199 are elevated in young *B6.Sst1S* and aged WT B6 mice compared to young WT B6 mice,
200 at a time point where no differences in CFU or histopathology are detected. These data
201 indicate that emergence of senescent cells precedes the failure of *Mtb* containment and
202 progression to necrosis in the TB-susceptible mice.

203 **'Omics studies show upregulation of the phosphatidylinositol 3-kinase (PI3K) and**
204 **the ERK1/2 cascades which are pro-survival, as well as certain anti-apoptotic**
205 **pathways in *Mtb*-infected BMDMs from *B6.Sst1S* mice.**

206 Senescent cells characteristically express cell cycle arrest and pro-inflammatory
207 transcriptional profiles[53,54,58]. To compare the gene expression in stressed *B6.Sst1S*
208 relative to young WT B6 BMDMs, we performed bulk RNA- sequencing with cells
209 subjected to TNFα stress, *Mtb* infection, or both (Figure 4A). BMDMs were exposed to
210 (1) only TNFα (10 ng/ml; 48 h), (2) only *Mtb* infection (MOI=1, 24 h), or (3) 10 ng/ml TNFα
211 pretreatment, followed by *Mtb* infection in the continued presence of TNFα (Figure 4A).
212 Despite increased *Mtb* proliferation in TNFα-treated *B6.Sst1S* BMDMs, cell viability
213 remained intact across all groups (Figure S6A, S6B). When treated with "TNFα only" for

214 48 h, we identified 1116 DEGs (*p.adj.*< 0.05, log2fold change >1 or <-1) with 597
215 upregulated and 519 downregulated genes in *B6.Sst1S* relative to similarly treated WT
216 B6 BMDMs (Supplementary File S3). In line with previous data, gene ontology (GO)
217 analysis for biological processes identified- cellular response to interferon-β
218 (GO:0035458; *p.adj.*< 1e-9), defense response to virus (GO:0051607; *p.adj.*< 1e-9),
219 cellular response to interferon-gamma (GO: 0071346; *p.adj.*= 2e-5), and innate immune
220 response (GO: 0045087; *p.adj.*= 1e-5) to be significantly enriched in the *B6.Sst1S*
221 BMDMs (Figure 4B, Supplementary File S3). Interestingly, a distinct transcriptome was
222 observed in *Mtb*-infected *B6.Sst1S* BMDMs (MOI=1; 24 h) (Figure 4B) characterized by
223 940 DEGs (*p.adj.*< 0.05, $\log_2$fold change >1 or <-1) with 455 upregulated and 485
224 downregulated genes in *B6.Sst1S* relative to similarly treated WT B6 BMDMs
225 (Supplementary File S4). Gene ontology (GO) analysis for biological processes identified
226 positive regulation of epithelial cell proliferation (GO:0050679; *p.adj.*= 7.97e-6), positive
227 regulation of PI3K signaling (GO:0014068; *p.adj.*= 1.6e-5), angiogenesis (GO:0001525;
228 *p.adj.*= 1.6e-5), positive regulation of IL-6 production (GO:0032755; *p.adj.*= 0.007), and
229 negative regulation of extrinsic apoptotic signaling (GO:2001240; *p.adj.*= 0.007) to be
230 significantly enriched in the *Mtb*-infected *B6.Sst1S* BMDMs (Figure 4B, Supplementary
231 File S4). The third group (exposure to both Tnfα and *Mtb*) showed 1177 DEGs (*p.adj.*<
232 0.05, $\log_2$fold change >1 or <-1) with 647 upregulated and 530 downregulated genes in
233 *B6.Sst1S* relative to similarly treated WT B6 BMDMs (Supplementary File S5). Gene
234 ontology (GO) analysis for biological processes identified receptor tyrosine kinase (RTK)
235 signaling pathway (GO:0007169; *p.adj.*= 0.006), positive regulation of PI3K signaling
236 (GO:0014068; *p.adj.*= 0.001), angiogenesis (GO:0001525; *p.adj.*= 6.34e-5), positive

237 regulation of cell proliferation (GO:0008284; *p.adj.*= 0.001) and apoptotic processes
238 (GO:0043065; *p.adj.*= 0.03), neutrophil chemotaxis (GO:0030593; *p.adj.*= 0.003), and
239 positive regulation of ERK1 and ERK2 cascade (GO:0070374; *p.adj.*= 0.005) to be
240 significantly enriched in the *B6.Sst1S* BMDMs (Figure 4B, 4C, Supplementary File S5).
241 As expected, the genes absent in *B6.Sst1S* cells (*Sp140, Sp110*) were among the top
242 downregulated genes in *B6.Sst1S* BMDMs (Figure 4C). Interestingly, we observed cyclin-
243 dependent kinase inhibitor *Cdkn1c,* senoantigen *Gpnmb*[59] and several genes included in
244 SenMayo[56] gene set (*Arg2, Ptger2, Iqgap2, Selplg, Mmp10, Mmp12, Gem, Ets2*), to be
245 upregulated in *B6.Sst1S* BMDMs (Figure 4C). Therefore, stressed *B6.Sst1S* BMDMs
246 exhibited upregulation of pro-survival pathways (PI3K-ERK1/2/MAPK cascade), enriched
247 SASP production (Metascape analysis; Log(*q*-value)= -15.49), and SASP expression
248 regulatory pathways (RTKs), which are characteristic of senescent cells. Additionally,
249 these cells showed increased expression of anti-apoptotic genes (Bcl2a1b, Bcl2a1d,
250 Itga6, Tnfaip8), suggesting resistance to apoptosis. Together, these changes suggest that
251 *Mtb*-infection and/or TNFα stress promotes macrophage entry into a long-lived and non-
252 dividing state characteristic of senescence.

253 **Therapy with senolytic drugs which kill senescent cells improves host survival**
254 **during *Mtb*-infection in *B6.Sst1S* mice.**

255 A potential strategy to combat aging has been to employ senolytic drugs designed to kill
256 senescent cells and reverse their SASP-mediated local deleterious effects. Indeed,
257 several senolytic drugs have been shown to prolong lifespan in rodent models,[60] and
258 reduce age-associated disease morbidity in human clinical trials.[21,58,61–63] We selected a
259 cocktail of three of the best-characterized senolytic agents: dasatinib (D), quercetin (Q),

260 and fisetin (F).[64] Dasatinib is a tyrosine kinase inhibitor active against Src family and other
261 tyrosine kinases.[65] Inhibiting multiple kinases promotes apoptotic cell death in senescent
262 cells by disrupting pro-survival signaling networks such as the PI3K, ERK1/2, and other
263 MAPK pathways.[60] Quercetin and fisetin are flavonoid antioxidants found in common
264 fruits and vegetables; they inhibit both the anti-apoptotic BCL-2 pathway and the pro-
265 survival PI3K and ERK1/2 pathways.[66–69] Because these pathways are up-regulated in
266 *Mtb*-infected *B6.Sst1S* macrophages (Figure 4B,4C), we reasoned that selectively
267 targeting senescent myeloid cells within TB lung lesions with the DQF cocktail would
268 contain intracellular *Mtb* growth.

269 First, we confirmed that D, Q, and F do not exert direct anti-microbial activity against *Mtb*
270 at pharmacologically relevant concentrations (Figure S7A, S7B). We then evaluated the
271 host-directed effect of DQF alone or DQF in combination with partial antimicrobial therapy
272 (comprised of ethambutol and rifampicin (DQF + Eth/Rif + Eth)) following an aerosol *Mtb*
273 infection that implanted 91 CFU on day 1 (Figure 5A, 5B). Our rationale for co-
274 administering antimicrobials was to prolong mouse survival giving a longer time window
275 to observe the impact of the host-directed drugs. One week of rifampin (bactericidal) was
276 intended to bring lung CFU counts down to ~6 $\log_{10}$ units, and 4 weeks of ethambutol
277 (bacteriostatic) was intended to extend survival with stable high lung CFU burden. Three
278 weeks post-infection, when the lung CFU burden was 7.18 $\log_{10}$CFU units (Figure 5B),
279 young *B6.Sst1S* mice were randomly apportioned to four oral gavage treatment groups
280 for a period of 28 days: (i) vehicle, (ii) DQF (d21-49), (iii) Eth/Rif (d21-28) + Eth (d29-49)
281 and (iv) DQF (d21-49) +Eth/Rif (d21-28) + Eth (d29-49) (Figure 5A). Compared with
282 vehicle, mice receiving DQF alone showed a trend towards prolonged survival in a subset

283 of mice (p= 0.09) with a certain degree of weight stabilization (Figure 5C, 5D). Mice
284 receiving DQF and partial antimicrobial therapy (DQF +Eth/Rif + Eth) showed a median
285 time to death (MTD) of 98 days and displayed significantly more weight gain (by 10-15%)
286 in comparison to those receiving partial antimicrobial therapy alone (Eth/Rif + Eth, MTD
287 of 68 days, p= 0.05) (Figure 5C, 5D). As has been noted by our group and others,[34,38,40,70]
288 *B6.Sst1S* mice infected with this *Mtb* challenge dose display a bimodal mortality curve
289 irrespective of therapeutic intervention, with 40-50% of all animals succumbing over the
290 first 35 days, and thus the impact of our drug regimens was only apparent in the remaining
291 50-60% of surviving mice.

292 **The DQF senolytic drug cocktail reduces *Mtb* proliferation and improves lung**
293 **pathology in young *B6.Sst1S* and aged WT B6 mice.**

294 Next, we evaluated the anti-TB effect of the DQF cocktail with or without Eth-antimicrobial
295 therapy in a lung CFU burden study of young *B6.Sst1S*, aged WT B6, and young WT B6
296 mice, following a low-dose *Mtb* aerosol challenge. (A low challenge dose was selected to
297 ensure that vehicle-treated *B6.Sst1S* mice would survive until the experimental endpoint).
298 In this experiment we started drug treatment at a later time point for WT B6 mice (4 wpi)
299 than for young *B6.Sst1S* and aged WT B6 (2 wpi) as shown in Figure 5E based upon our
300 prior observations that WT B6 mice showed lower levels of senescence markers at early
301 timepoints and were better able to contain *Mtb* proliferation than the other two groups.
302 Compared to the vehicle-treated group, DQF therapy reduced lung CFU counts in
303 *B6.Sst1S* mouse lungs by 1.3 (p= 0.12) and 2.2 (p= 0.16) $\log_{10}$CFU units at 5 and 8 wpi,
304 respectively, and in aged WT B6 mouse lungs by 0.5 (p= 0.11) $\log_{10}$ units at 5 wpi (Figure
305 5F), but none of these reductions were statistically significant. We did not find a detectable

306 difference in lung CFU counts of young WT B6 mice at 8 wpi (Figure 5F). The addition of
307 ethambutol to DQF host-directed therapy significantly lowered lung CFU counts in all
308 mouse strains compared to ethambutol monotherapy; however, the magnitude of the
309 reduction was most profound in *B6.Sst1S* mice at 0.31(p= 0.02) and 1.0 (p=0.07)
310 $\log_{10}$CFU units at 5 and 8 wpi, respectively, and in aged WT B6 mice at 0.6 $\log_{10}$CFU (p=
311 0.01) units at 5 wpi (Figure 5F). The difference in treatment times between mice strains
312 precluded us from comparing outcomes across groups. However, in the given
313 experimental conditions, young WT B6 mice also showed a reduction of 0.3 $\log_{10}$CFU
314 units at 8 wpi (p=0.006) upon adding DQF to ethambutol (Figure 5F). With spleen CFU
315 counts, the addition of DQF to ethambutol lowered the bacterial burden in *B6.Sst1S* mice
316 by 1.0 and 0.6 $\log_{10}$CFU units at 5 (p=0.24) and 8 wpi (p=0.02), respectively. In case of
317 aged WT B6 mice, spleen CFU burden was reduced by 1.1 $\log_{10}$CFU units at 5 wpi (p=
318 0.0001) compared to ethambutol alone (Figure 5G). There was no significant reduction
319 observed between these groups for young WT B6 mice (Figure 5G).

320 Next, we examined whether lung immunopathology is altered by senolytic drug therapy
321 in the above experimental setup. In line with previous studies, necrotic granulomas were
322 observed in 3 out of 6 (50%) *B6.Sst1S* mice at 5 wpi, and 3 out of 5 (60%) mice at 8 wpi
323 (Figure S8A, S8B). Treatment with DQF alone delayed the emergence of necrotic
324 granuloma formation, as necrotic granuloma was observed in 1 out of 6 mice (17%) and
325 in none of the 5 mice (0%) at 5 and 8 wpi, respectively (Figure S8A, S8B). Additionally,
326 treatment with bacteriostatic drug Eth alone also resolved lung pathology and none of the
327 mice exhibited necrosis (Figure S8A, S8B). Next, we measured the percentage area (of
328 the lung) of consolidated lesions on H&E-stained histology slides (Figure 6A). All three

329 mouse strains showed greatest reductions in percent lesion area in the DQF+ Eth-
330 treatment group as compared with the vehicle group (*B6.Sst1S*: *p*= 0.02, aged WT B6:
331 *p*= 0.07, and young WT B6: *p*= 0.04) (Figure 6A). While DQF alone prevented the
332 formation of necrotic granuloma in *B6.Sst1S* mice, no statistically significant difference in
333 percent lesion area was observed (Figure 6A). Additionally, the overall degree of lung
334 consolidation remaining (percent lesion area) was improved in DQF+ Eth-treated
335 *B6.Sst1S* (5 wpi- ≈5-fold, 8 wpi- ≈4-fold) and aged WT B6 mice (5 wpi- ≈2-fold) relative to
336 the vehicle-treated mice (Figure 6A, Figure S8, S9A). In the case of young WT B6 mice,
337 Eth alone was insufficient to improve the lung pathology at 8 wpi. However, DQF alone
338 (22%; *p*= 0.001) and DQF+Eth (26%; *p*= 0.04) treatment significantly reduced the
339 percentage lung lesion area relative to the Veh group (37%) (Figure 6A).

340 In sum, CFU and histology data suggest that the DQF senolytic drug cocktail can act as
341 a valuable host-directed therapy in both young *B6.Sst1S* and aged WT B6 mouse TB
342 models.

343 **The DQF cocktail reduces senescence markers in *Mtb*-infected lungs of young**
344 ***B6.Sst1S* and aged WT B6 mice.**

345 To determine if the improved survival, *Mtb* containment, and lung pathology observed in
346 DQF-treated mice correlated with the removal of senescent cells, we evaluated markers
347 of senescence (γH2A.x, p21, p16 and SA-βGal activity) in mouse lungs for the 3
348 categories of mice treated as in Figure 5E. Immunohistochemistry for the DNA damage
349 marker γH2A.X showed no significant differences in immunoreactivity across mice strains
350 between DQF-alone treated and vehicle-treated mice, but in aged WT mice (*p*=0.049)
351 (Figure 6B, Figure S9B). Interestingly, Eth treatment reduced DNA damage area of the

352 lung by 4-fold only in *Mtb*-infected *B6.Sst1S* mice at 5 wpi (Figure 6B); however, this effect
353 was not seen at 8 wpi (Figure S9B). Moreover, Eth-treated young or aged WT B6 mice
354 exhibited similar γH2A.X-immunoreactivity relative to the vehicle group (Figure 6B).
355 Importantly, the highest reduction of DNA damage was observed in DQF+ Eth-treated
356 *B6.Sst1S* (≈80-fold at 5 wpi relative to the vehicle group) and aged WT B6 mice (≈2-fold
357 at 5 wpi relative to the vehicle group) with mice receiving both drugs showed a near
358 absence of any γH2A.X-stained lung area (Figure 6B, Figure S9B). In terms of the
359 intensity of γH2A.X-staining, the highest reduction of DNA damage was also observed in
360 DQF+ Eth-treated *B6.Sst1S* with a ≈350-fold reduction at 5 wpi relative to the vehicle
361 group, and ≈4-fold lower for aged WT B6 mice at 5 wpi (Figure 6C).

362 Notably, when we evaluated the live lung cells by flow cytometry for dual staining with
363 $p21^{+}\beta Gal^{+}$ and for $p16^{+}\beta Gal^{+}$ (Figure S4), there were significant reductions in both pairs
364 of senescence markers in the DQF alone group and in the DQF+ Eth group for young
365 *B6.Sst1S* and aged WT B6 mice (Figure 7A, 7B Figure S9C, S9D). Eth monotherapy
366 reduced $p21^{+}\beta Gal^{+}$ and $p16^{+}\beta Gal^{+}$ population by ≈10-fold in *B6.Sst1S* mice lung at 5 wpi,
367 indicating that inhibiting *Mtb* replication can also impede the generation of p21+βGal+ or
368 for p16+βGal+ cells (Figure 7A, 7B). Interestingly, DQF alone also reduced the $p21^{+}\beta Gal^{+}$
369 and for $p16^{+}\beta Gal^{+}$ by ≈4-fold relative to the vehicle group in *B6.Sst1S* mice, and we did
370 not see further reduction of $p21^{+}\beta Gal^{+}/p16^{+}\beta Gal^{+}$ population when DQF was added to
371 the Eth monotherapy (Figure 7A). In the case of aged WT B6 mice, while Eth
372 monotherapy was ineffective (p>0.05), DQF+ Eth significantly reduced the senescence
373 markers in the mice lung (Figure 7B). In contrast, we saw no changes for dual positivity
374 in young WT B6 mice with any of the DQF and/or Eth regimens compared to vehicle-

375 treated group (Figure 7C). The lung cells showing the highest reductions in dual positivity
376 upon DQF or Eth treatment for p21+βGal+ or for p16+βGal+ were predominantly from the
377 CD45+myeloid lineage cells (Figure 7D, 7E).

378 In summary, the senolytic drug cocktail DQF prolonged survival, lowered lung CFU
379 counts, and pathology concomitant with a reduction in senescence markers in TB-infected
380 mice (Figure 7F). The greatest host-beneficial effects were observed in TB-susceptible
381 young *B6.Sst1S* and aged WT B6 mice.

382

383

384

385

386

387

388

389

390

391

392

393

394 **Discussion**

395 This study provides proof of concept data that lung myeloid cells acquire a senescence
396 phenotype during TB and that these senescent cells contribute to disease progression.
397 In this work, we first used BMDMs to establish that TNFα treatment in aged WT B6 and
398 young *B6.Sst1S* BMDMs are not only associated with poorer *Mtb* containment but also
399 the induction of classical senescence markers including SA-βGal, SASP gene
400 expression, cell cycle arrest (reduced BrdU incorporation, Lamin B1 and increased p16),
401 and DNA damage (γH2A.X). Our previous work with the *B6.Sst1S* macrophages revealed
402 up-regulation of many SASP genes (*Il6, Ccl2, Cxcl11, Tgfβ3, Mmp13, Tnfsf10*)
403 (Supplementary File S1) and induction of the anti-apoptotic ISR pathway after TNFα-
404 stimulation at an early time point (18 hours).[38] Using *Mtb*-infected aged WT B6 mice as a
405 benchmark, we sought to determine whether young *B6.Sst1S* mice resembled aged WT
406 B6 or young WT B6. Our studies revealed that both young *B6.Sst1S* mice-lungs and their
407 BMDMs displayed the same panel of senescence markers during stress (TNFα) or *Mtb*
408 infection as observed in aged WT B6 samples. The senescence phenotypes seen in the
409 *B6.Sst1S* model resembled those of aged WT B6 samples to a much greater degree than
410 those of young WT B6. These data suggest that after *Mtb* infection, *B6.Sst1S* mice exhibit
411 accelerated myeloid cell senescence, and that this may contribute to their unique
412 development of necrotic granulomas.

413 Advanced age is a well-known TB risk factor,[7,62,63] where early mouse studies by Orme
414 and Turner showed that *Mtb*-infected old mice have accelerated lethality post-*Mtb*
415 challenge.[14,71,72] The macrophages in aged mice were *Mtb*-infected in higher numbers
416 and expressed higher levels of the IFN-I responsive genes IRGM-1 and IRF-1.[73]

417 Interestingly, DiNardo *et al.* recently found that active TB leads to accelerated aging in
418 humans and in a guinea pig acute TB model using the DNA methylation clock.[74,75] Using
419 combined hypermethylation and gene expression clock algorithms, they found that active
420 TB adds 12.7 years (by the Horvath DNA hypermethylation clock) or 14.4 years (by the
421 Transcriptomic 'RNAAgeCalc' clock) of cellular aging compared to latent TB-infected
422 humans (LTBI).[74] Consistent with this, TB patients have been reported to show
423 significantly shorter telomere length and increased mitochondrial DNA copy number
424 (markers of senescence) relative to healthy controls in a diverse population.[76–78]
425 Additional studies have indeed demonstrated that *Mtb* infection induces DNA damage,
426 manipulates host cell cycle checkpoints, and promotes senescence-like features in
427 macrophages,[79–82] or T cells.[83]
428 The senescence literature has demonstrated that pathways required for homeostatic
429 development and wound healing in young age become dysregulated during aging.[30]
430 These include fibrosis with stem cell exhaustion in the setting of chronic mTOR activation,
431 persistent inflammation with excessive SASP cytokine release due to chronic NF-κB
432 activation, DNA damage and mitochondrial dysfunction in the setting of declining sirtuin
433 activity.[84,85] A hallmark of senescent cells is entry into a non-dividing, long-lived state with
434 chronic expression of locally deleterious and immunosuppressive signals that promote
435 age-associated disease processes. In TB, the majority of infected humans adequately
436 contain *Mtb* infection within immune-balanced quiescent lung granulomas. We propose
437 that in TB-susceptible hosts, such as *B6.Sst1S* mice (interferonopathy) or aged WT B6
438 mice (aging/inflammaging), a subset of stressed myeloid cells transit into a stress-induced
439 senescent (SIS) state characterized by growth arrest and local secretion of SASP factors.

440 These SASP molecules include type I interferon, PD-L1, IL-1 receptor antagonist,[34] IL-
441 10, IL-6, CCL2, and GM-CSF. These senescent myeloid cells, via SASP secretion, may
442 promote chronic local inflammation and recruit immunosuppressive myeloid-derived
443 suppressor cells (MDSCs) into granulomas.[25,26,86] We indeed observed several canonical
444 immunoregulatory molecules that can collectively dampen antimicrobial immunity, to be
445 upregulated in the cells neighboring to non-controlling lesions in *B6.Sst1S* mice
446 (Supplementary File S2). Among the upregulated DEGs, Checkpoint receptors or ligands
447 such as Pdcd1 (PD-1; T-cell exhaustion), Cd274 (PD-L1), Fcgr2b, Cd33, Ceacam1,
448 Sirpb1a and Tnfrsf1b can prevent T cell activation. Metabolic and enzymatic brakes,
449 including Arg1, Arg2, Nos2, Il4i1, Ptgs2, Acod1, Hmox1 and the adenosine receptor
450 Adora2b, constrain lymphocyte proliferation by depleting arginine or generating
451 immunomodulatory metabolites. Signal-terminating proteins Socs3, Nlrp12, Dusp1, and
452 the IL-1 antagonist Il1rn attenuate JAK/STAT, NF-κB or MAPK cascades, whereas
453 chemokines- Ccl2,Ccl3, Cxcl1, Cxcl2 and S100A8/S100A9-alarmin can recruit
454 MDSCs,[87–89] reinforcing a suppressive milieu locally in the tissue (Supplementary File
455 S2). In turn, it has been shown that MDSCs further sustain immunosuppression by
456 secreting IL-10, TGF-β, and reactive oxygen species (ROS), impairing effective cytotoxic
457 T-cell and NK-cell responses and preventing clearance of senescent cells.[27] These
458 paracrine signals also feed the cycle of IFN-I hyperexpression in uninfected bystander
459 cells, blunt T cell activation,[44] and recruit additional immature myeloid cells leading to
460 granuloma progression. Consequently, SIS myeloid cells and recruited MDSCs may
461 collectively shape an immunosuppressive granuloma microenvironment favorable to *Mtb*

462 replication, while impeding the establishment of protective immune control, as seen in
463 cancer-biology.

464 We found that senescence markers in aged WT B6 and young *B6.Sst1S* appear as early
465 as 10 days after *Mtb* infection, well before the appearance of granuloma formation and
466 lung immunopathology. This early chronology suggests that myeloid cell senescence may
467 be a contributory driver of the more severe TB pathology in aged WT B6 and young
468 *B6.Sst1S* animals. To establish causality, we used a cocktail of the senolytic drugs
469 dasatinib, quercetin, and fisetin (DQF) which eliminate senescent cells by inhibiting the
470 kinase (RTK/ PI3K/ ERK)-dependent survival pathways and anti-apoptotic mechanisms
471 that sustain their long-lived, non-dividing state. These drugs have been shown to prolong
472 lifespan in rodents and to prevent the progression of age-associated diseases in
473 humans.[21,58,60,61] We found that the DQF cocktail with or without partial antimicrobial
474 therapy was sufficient to prolong mouse survival and reduce *Mtb* organ burden. Moreover,
475 the impact of the senolytic DQF cocktail was more prominent in mice that showed
476 elevated senescence markers during *Mtb* infection, namely young *B6.Sst1S* and aged
477 WT B6 mice. The fact that senolytic drugs improve TB disease outcome parameters is a
478 potent argument that senescent lung myeloid cells contribute to TB progression in these
479 animal models. As major risk factors for TB (age, malnutrition, diabetes, pollution, and
480 smoking) have been shown to induce senescence,[72,90–95] this study correlating senescent
481 cells with TB progression may also offer a mechanistic link for how these human risk
482 factors promote TB progression. Interestingly, we also observed that treatment with the
483 bacteriostatic drug ethambutol reduced the accumulation of senescence markers. This
484 supports the established notion that chronic lung inflammation resulting from persistent

485 *Mtb* growth can indeed induce stress-induced senescent (SIS) cells. Taken together, our
486 findings suggest that TB susceptibility factors promote a lung environment favorable for
487 *Mtb* replication, fueling a self-amplifying/feed-forward cycle of senescence and
488 inflammation, ultimately driving progression toward necrotic granulomas.

489 Considerable recent attention has been directed to the problem of post-TB lung disease.
490 Despite adequate and durable cures, many TB patients are left with serious pulmonary
491 disease, including bronchiectasis and either obstructive or restrictive lung disease.[96–99]
492 Senescent cells have been strongly associated with chronic tissue inflammation and
493 inappropriate fibrotic scarring.[100] Our studies with senolytic drugs indicated that lung
494 immunopathology was reduced to a greater degree by senolytic drugs in young *B6.Sst1S*
495 and aged WT B6 mice, which have high senescent cell burdens. Thus, in addition to
496 serving as promising adjunctive host-directed therapies for active TB, senolytic drugs may
497 also reduce post-TB lung disease. In summary, this demonstration of senolytic drug
498 efficacy mouse TB models offer a rationale for testing senescence-targeting strategies in
499 human TB clinical trials.

500

501

502

503

504

505

506 **Material and Methods**

507 **Animals used in this study.**

508 Young C57BL/6J female mice (6 weeks old; Strain: 000664) and Aged C57BL/6J females
509 (>68 weeks old) were bought from The Jackson Laboratory (Bar Harbor, ME, USA). The
510 B6.C3H-sst1(B6J.C3-sst1C3HeB/FejKrmn) congenic mice were generated previously by
511 transferring the *sst1S* allele from C3HeB/FeJ mouse strain to the B6 (C57BL/6J) genetic
512 background using 12 backcrosses (*B6.Sst1S*)[32,38] and confirmed by Genotyping. The
513 oligonucleotides used for the PCR are shown in Supplementary File S6. This mice strain
514 was bred and maintained at the Rodent Vivarium of Johns Hopkins University, School of
515 Medicine and was used in this study. All experiments were conducted under protocols
516 approved by the Johns Hopkins Animal Care and Use Committee (Protocol Number:
517 MO22M466) and followed established ethical animal handling and care guidelines.
518 Animals were housed in individually ventilated cages under controlled conditions,
519 including a 12-hour light/dark cycle, ambient temperatures ranging from 20 to 24°C, and
520 relative humidity between 45% and 65%. Each cage contained no more than five mice of
521 the same strain/sex to ensure proper animal welfare. Mice were randomly assigned to
522 experimental groups to minimize bias. Humane and painless euthanasia procedures were
523 employed in compliance with AVMA (American Veterinary Medical Association)
524 guidelines.

525 All experiments involving *Mycobacterium tuberculosis* H37Rv were conducted in
526 Biosafety Level 3 (BSL3) and Animal Biosafety Level 3 (ABSL3) facilities at the Johns
527 Hopkins University, School of Medicine, following protocols approved by the Institutional
528 Biosafety Committee. Aerosol infections were performed using a Glas-Col aerosolization

529 system, allowing the mice to move freely in the chamber and minimizing stress or
530 discomfort. Anesthesia was not required for this procedure. Mice were briefly restrained
531 during oral gavage to ensure accurate delivery. Infected animals were monitored for signs
532 of illness, such as weight loss or lethargy, and those that became moribund before the
533 experiment's conclusion were promptly euthanized, except in survival studies.

534 **BMDMs isolation, culture, and treatment with murine-TNFα.**

535 BMDMs were isolated from mice at the indicated age, as described previously[101]. Briefly,
536 BMDMs were isolated from the tibias and femurs of mice and were differentiated into
537 macrophages in RPMI-Glutamax (Thermo Fisher Scientific; 61870127) containing 10%
538 heat-inactivated FBS (Millipore Sigma, Catalog no.- F4135), 1X antibiotic-antimycotic
539 Solution (Sigma Aldrich; A5955) and 10% (v/v) L929 fibroblast-conditioned medium (as a
540 source of M-CSF(macrophage colony-stimulating factor)) for 5 days. L929 fibroblast cell
541 lines were cultured in DMEM-Glutamax (Thermo Fisher Scientific; 10566016) containing
542 10% heat-inactivated FBS, 10 mM HEPES, and 1X antibiotic- antimycotic Solution. L929
543 cells were mycoplasma-negative (Venorgem Mycoplasma detection kit; Millipore Sigma-
544 MP0025). BMDMs were either left untreated or treated with 10 ng/ml of murine-TNFα
545 (Peprotech; 315-01A) in RPMI-Glutamax containing 10% heat-inactivated FBS and 10%
546 (v/v) L929 fibroblast-conditioned medium, for indicated time durations at 37°C in 5% CO_2.
547 BMDMs were washed, scraped out, counted, and replated overnight prior to the
548 experiments. All experiments were done with confluency of BMDMs 60-75%.

549 **Senescence associated β-Galactosidase assay (SA-βGal assay).**

550 SA-βGal assays at indicated time points were done with both paraformaldehyde- fixed
551 (Senescence Cells Histochemical Staining Kit; Sigma; CS0030) and live BMDMs
552 (Senescence β-Galactosidase Activity Assay Kit (Fluorescence, Flow Cytometry); Cell
553 Signaling Technology; 35302), using a modified manufacturer's protocol. At indicated time
554 points, BMDMs were washed twice with PBS and fixed with 1X fixation buffer for 10
555 minutes. BMDMs were washed thrice, the staining mixture was added to each well and
556 incubated for 48 h at 37°C without CO_2. We used 0.04X the X-gal Solution (10 µl in 1ml
557 of Staining mixture), to avoid saturation of the signal. The plate was sealed with Parafilm
558 to prevent evaporation of the staining mixture. After the incubation, cells were observed
559 under a bright field microscope and images were captured from the center of the well.

560 For experiments with live cells, adherent BMDMs were washed twice with warm PBS, and
561 incubated in Bafilomycin A1 (freshly prepared; 100 nM) containing complete RPMI
562 medium for 2 hours. Next, 0.05X of the recommended concentration of the SA-βGal
563 Substrate Solution (0.66 µM) was added to the cells and incubated for another 2- 2.5
564 hours at 37°C and 5% CO_2. The cells were washed thrice with PBS, scraped out in 1ml
565 RPMI (without phenol red) (Gibco; 11835), and LIVE/DEAD Fixable Near-IR Dead Cell
566 Stain (Thermo Fisher Scientific; L10119) was added for the detection of dead cells. FACS
567 was immediately done using CytoFLEX cytometer (Beckman Coulter), and 10000
568 events/sample were recorded. BMDMs from aged WT B6 mice (>72 weeks) were used
569 as a positive control. For etoposide (Millipore Sigma; E1383)- induced senescence
570 control, WT B6 BMDMs were treated with 10 µM etoposide for 2 days in complete RPMI
571 media, followed by washing to remove DNA-damaging molecules, and further incubation

572 for 2 days, in complete RPMI media only (no loss of viability under these conditions, as
573 detected by Alamar HS assay).

574 **Cell viability assay.**

575 The viability of cells was measured using an Alamar Blue HS Cell Viability Reagent
576 (Thermo Fisher Scientific; A50100), according to the manufacturer's protocol. Briefly, at
577 the indicated point, the (warmed) viability reagent was added to each well at 1/10th the
578 volume of cells, incubated for 6-8 hours and the fluorescence intensity was measured
579 using a FLUOstar Omega Multidetection Microplate Reader (BMG Labtech) in the bottom-
580 reading mode with excitation at 544 nm and emission at 590 nm. Untreated cells and cells
581 treated with 0.06% SDS, were used as positive and negative control, respectively.
582 Percent viability was calculated from the relative fluorescence units compared with
583 positive and negative control cells, to which the experimental values were normalized.

584 **Isolation of RNA and quantitative RT-PCR analysis to detect SASP expression.**

585 At the indicated time points, BMDMs were lysed in TRIzol (Thermo Fisher Scientific;
586 15596026), and RNA was extracted using Qiagen RNeasy Mini Kit (74104) and RNase-
587 free DNase Set (Qiagen; 79254), following the manufacturer's protocol. RNA purity and
588 concentration were quantified using Nanodrop One (Thermo Fisher Scientific). 1 µg of
589 RNA was used for cDNA synthesis using the iScript cDNA Synthesis Kit (BioRad;
590 1708891) and quantitative RT-PCR was done with QuantStudio 3 (Applied Biosystems;
591 Thermo Fisher Scientific) using gene-specific primers (Supplementary File S6) and iTaq
592 Universal SYBR Green Supermix (BioRad; 1725121). Expression of genes was
593 normalized with Ct value for *ActB* (internal housekeeping control).

594 **BrdU Cell proliferation assay.**

595 The capacity of BMDMs to proliferate was measured by using the BrdU Cell Proliferation
596 Assay Kit (Cell Signaling Technology; 6813), following the manufacturer's protocol.
597 Briefly, 1-day post seeding of 50000 BMDMs in a 48-well plate, growth media (RPMI-
598 Glutamax+ FBS) was removed, and RPMI-only was added to the cells to synchronize
599 their cell cycle (upon serum starvation) and incubated for 18 hours at 37°C and 5% CO_2.
600 After this synchronization-step, complete RPMI media was added to all wells and
601 incubated for another 24 hours. The cells were either left untreated or treated with 10ng/ml
602 TNFα, and BrdU incorporation into the cells was measured following the manufacturer's
603 recommendations. Treatment of WT B6 BMDMs with 10 μM etoposide acted as a positive
604 control. Absorbance at 450 nm was measured using the Bio-Rad iMark microplate reader.

605 **Protein isolation and Western Blotting.**

606 BMDMs were washed twice with ice-cold PBS, and the total protein was extracted by
607 lysing cells in radioimmunoprecipitation (RIPA) Buffer (Millipore Sigma; R0278) containing
608 Protease/Phosphatase Inhibitor Cocktail (1X; Cell Signaling Technology; 5872). After
609 incubating on ice for 15 min with gentle vortexing, the lysates were centrifuged at 14000
610 RPM, 4°C for 15 min. The clarified supernatant was taken, and protein concentrations
611 were quantified using the BCA Assay kit (Thermo Fisher Scientific; 23225). Approximately
612 50 μg of protein were mixed with Laemmli sample buffer (Bio-Rad; 1610747) and heated
613 at 95 °C for 5 min before loading onto 4-15% MP TGX polyacrylamide Gel (Bio-Rad;
614 45610848) and transferring to the PVDF membranes (Bio-Rad; 1620177). The PVDF
615 membranes were blocked using 5% Blotting-grade blocker (Bio-Rad; 1706404) in TBST
616 buffer- Tris-buffered saline (Quality Biological; 351086101)+ 0.1% Tween 20 (Sigma;

617 P2287) for 1-2 hour and incubated overnight at 4ºC with the primary antibodies from
618 Mouse Reactive Senescence Marker Antibody Sampler Kit (Cell Signaling Technology-
619 78551)- Phospho-Histone H2A.X (Ser139) (20E3) Rabbit mAb (1: 1000 dilution), Lamin
620 B1 (E6M5T) Rabbit mAb (1: 1000 dilution), HMGB1 (D3E5) Rabbit mAb (1: 1000 dilution),
621 p16 INK4A (E5F3Y) Rabbit mAb (1: 1000 dilution) and β-Actin (D6A8) Rabbit mAb (Cell
622 Signaling Technology; 8457) (1:5000 dilution). Following three 15 min washing steps with
623 TBST, the membranes were incubated with secondary antibody- Anti-rabbit IgG, HRP-
624 linked Antibody (1:1000 dilution) for 2 hours at room temperature (RT). Following three
625 15 min washing steps, the membranes were developed with Pierce™ ECL Western
626 Blotting Substrate (Thermo Fisher Scientific; 32109) and visualized using a KwikQuant
627 Digital Western Blot Detection System (Kindle Bioscience; D1001). Images were
628 processed in Adobe Photoshop Software. Stripping Buffer (Restore™ Western Blot
629 Stripping Buffer; Thermo Fisher Scientific; 21059) was used to redevelop PVDF
630 membranes, following the manufacturer's protocol.

631 **Bulk RNA-Sequencing and analysis.**

632 BMDMs were lysed in TRIzol (Thermo Fisher Scientific; 15596026), and RNA was
633 extracted using Qiagen RNeasy Mini Kit (74104) and RNase-free DNase Set (Qiagen;
634 79254), following the manufacturer's protocol. RNA purity and concentration was
635 quantified using Nanodrop One (Thermo Fisher Scientific) and stored at -80 ºC. RNA
636 samples were shipped on dry ice to Genewiz, Azenta Life Sciences (South Plainfield, NJ,
637 USA) for standard bulk RNA- sequencing and downstream analysis. Sample QC, library
638 preparations, sequencing reactions, and initial bioinformatic analysis were conducted as
639 follows: Total RNA samples were quantified using Qubit 2.0 Fluorometer (Life

640 Technologies, Carlsbad, CA, USA) and RNA integrity was checked with 4200 TapeStation
641 (Agilent Technologies, Palo Alto, CA, USA). Samples were initially treated with TURBO
642 DNase (Thermo Fisher Scientific, Waltham, MA, USA) to remove DNA contaminants. The
643 next steps included performing rRNA depletion using QIAseq® FastSelect™−rRNA HMR
644 kit (Qiagen, Germantown, MD, USA), which was conducted following the manufacturer's
645 protocol. RNA sequencing libraries were generated with the NEBNext Ultra II RNA Library
646 Preparation Kit for Illumina by following the manufacturer's recommendations. Briefly,
647 enriched RNAs were fragmented for 15 minutes at 94°C. First strand and second strand
648 cDNA were subsequently synthesized. cDNA fragments were end-repaired and
649 adenylated at 3'ends, and universal adapters were ligated to cDNA fragments, followed
650 by index addition and library enrichment with limited cycle PCR. Sequencing libraries
651 were validated using the Agilent Tapestation 4200 (Agilent Technologies, Palo Alto, CA,
652 USA), and quantified using Qubit 2.0 Fluorometer (ThermoFisher Scientific, Waltham,
653 MA, USA) as well as by quantitative PCR (KAPA Biosystems, Wilmington, MA, USA). The
654 sequencing libraries were multiplexed and clustered on one lane of a flow cell. After
655 clustering, the flow cell was loaded on the Illumina HiSeq 4000 instrument according to
656 the manufacturer's instructions. The samples were sequenced using a 2x150 Pair-End
657 (PE) configuration. Image analysis and base calling were conducted by HiSeq Control
658 Software (HCS). Raw sequence data (.bcl files) generated from Illumina HiSeq was
659 converted into FASTQ files and de-multiplexed using Illumina's bcl2fastq 2.17 software.
660 One mismatch was allowed for index sequence identification.

661 Raw sequencing reads were trimmed to remove adapter sequences and low-quality
662 bases using Trimmomatic v0.36, and the filtered reads were aligned to the *Mus musculus*

663 GRCm38 reference genome (ENSEMBL) using the splice-aware STAR aligner v2.5.2b,
664 generating BAM files. Gene hit counts were quantified using featureCounts from the
665 Subread package v1.5.2, counting only uniquely mapped reads overlapping annotated
666 exon regions, with strand specificity applied where appropriate. Differential expression
667 analysis was performed using the DESeq2 package[102]. Genes with an adjusted *p*-value
668 <0.05 and a $\log_2$ fold change > 1 or <-1 were deemed differentially expressed between
669 groups. Statistically significant differentially expressed genes (DEGs) were analyzed for
670 biological process enrichment through gene ontology analysis using the software
671 GeneSCF v1.1-p2 with the MGI GO database, generating clusters of functionally relevant
672 GO terms. Raw data were deposited in NCBI's Gene Expression Omnibus (GEO,
673 accession number-GSE292458, GSE301446). Reviewers can access this data using the
674 following token number- ihyhoqmkbhwxxmp, cdybcgoyrbqhtap, respectively.

675 **Minimum inhibitory concentration (MIC) and Minimum bactericidal concentration**
676 **(MBC) determination against *Mycobacterium tuberculosis* H37Rv.**

677 *Mycobacterium tuberculosis* strain H37Rv (*Mtb*) was obtained from the Johns Hopkins
678 University, Center for Tuberculosis Research (CTBR) and sequence-verified regularly.
679 *Mtb* was grown in 7H9 broth supplemented with 0.2% glycerol, 0.05% Tyloxapol (Millipore
680 Sigma; T0307), and OADC (BD; 212351) with shaking at 180 rpm in a rotary shaker
681 incubator or on 7H11 agar supplemented with OADC at 37°C. MIC was determined by a
682 resazurin microtiter assay (REMA) using 96-well flat-bottom plates[103]. *Mtb* H37Rv was
683 cultured in 7H9+OADC medium and grown to an exponential phase (optical density at
684 600 nm = 0.6-0.8). Approximately 1×10^5 bacteria per well were added in a total volume
685 of 200 µL of 7H9+OADC medium. Wells lacking *Mtb* served as controls. Additional

686 controls consisted of wells containing *Mtb* cells without drug treatment (growth control).
687 After 5 days of incubation at 37°C in the presence of drugs, 30 µL of 0.02% resazurin
688 (Sigma-Aldrich; R7017) was added, and plates were incubated for an additional 24-48
689 hours. The fluorescence intensity was measured using a FLUOstar Omega Multidetection
690 Microplate Reader (BMG Labtech) in the bottom-reading mode with excitation at 544 nm
691 and emission at 590 nm. Percent inhibition was calculated from the relative fluorescence
692 units compared with an untreated control culture; the MIC was taken as the lowest drug
693 concentration that resulted in at least 90% reduction in fluorescence compared to the
694 untreated growth control. To determine the MBC, 20 µl of cells from the respective MIC
695 dilutions (from the 96-well plate) were added onto the 7H11+OADC agar plate. Following
696 8-10 days of incubation at 37 °C, the colonies were checked for *Mtb* growth. Three wells
697 each from media containing no inoculum and, media containing *Mtb* but no drug, were
698 used as blank and growth controls, respectively. MBC was defined as the lowest drug
699 concentration at which no *Mtb* colonies appeared on the 7H11 plates.

700 **Spatial Transcriptomics of Lung from *Mtb* infected *B6.Sst1S* mice.**

701 To characterize gene expression in controlled vs uncontrolled lesions, we performed
702 spatial transcriptomics analysis using the Nanostring GeoMX Digital Spatial Profiler
703 (DSP) system (Nanostring, Seattle, WA).[104,105] The lung sections we processed for spatial
704 transcriptomics were obtained from *B6.Sst1S* mice. We used 10^6 CFU of *Mtb* H37Rv for
705 infection, administered subcutaneously in the hock. The samples were collected at 14
706 weeks post-infection. Based on routine hematoxylin and eosin histopathology, we
707 selected lungs from 2 mice with paucibacillary controlled lesions and 2 mice with
708 advanced uncontrolled multibacillary lesions with necrotic areas. Additional FFPE

709 sections were stained with fluorescent CD45-, pan-keratin-specific antibodies and DAPI.
710 Diseased regions of interest (ROI) were selected to focus on myeloid-rich areas avoiding
711 necrosis and tertiary lymphoid tissue. Eight ROI each of controlled and uncontrolled
712 lesions (respectively) were studied. The profiling used the Mouse Whole Transcriptome
713 Atlas (WTA) panel which targets ~21,000+ transcripts for mouse protein coding genes
714 plus ERCC (External RNA Controls Consortium) negative controls to profile the whole
715 transcriptome, excluding uninformative high expressing targets such as ribosomal
716 subunits.

717 Samples from each ROI were packaged into library for sequencing (NextSeq550,
718 Illumina) following the procedure recommended by Nanostring. After sequencing, the
719 data analysis workflow began with QC evaluation of each ROI based on thresholds for
720 number of raw and aligned reads, sequencing saturation, negative control probe means,
721 and number of nuclei and surface area. Background correction is performed using
722 subtraction of the mean of negative probe counts. Q3 normalization (recommended by
723 Nanostring) results in scaling of all ROIs to the same value for their 3rd quartile value.
724 Statistical analysis was then performed to identify differentially expressed genes, using
725 an unpaired t-test with Benjamini-Hochberg adjustment for *p* values. Raw data were
726 deposited in NCBI's Gene Expression Omnibus (GEO, accession number- GSE292392).
727 Reviewers can access this data using the following token number- clozaycmjjivduj.

728 **Animal infection studies.**

729 Mice of the specified age and sex were infected via aerosol exposure using the Glas-Col
730 Inhalation Exposure System (Terre Haute, IN, USA). Fresh cryo-aliquots of *Mtb* H37Rv
731 were used for each infection, diluted in sterile 7H9 broth to empirically determined

732 concentrations to achieve the desired bacterial load on day 1 post-infection. To minimize
733 variability between groups, mice from all experimental groups were infected concurrently
734 and randomly allocated to experimental arms. The bacterial implantation in the lungs was
735 assessed one day after infection by sacrificing 3–5 mice per group and determining
736 colony-forming units (CFUs). Mice were euthanized at specified time points (as outlined
737 in the Results section), and the lungs and spleen were aseptically harvested, weighed
738 and either homogenized by bead-beating for bacterial quantification (Right lung) or stored
739 in 10% neutral-buffered formalin for histopathological analysis (Left lung). CFU
740 enumeration was performed by plating serial dilutions on 7H11 agar supplemented with
741 OADC, followed by incubation at 37°C for 3 to 4 weeks. Bacterial counts were normalized
742 to the weight of the total organ, as previously described[106].

743 **Histopathology to estimate lung inflammation.**

744 For histology, left lungs were fixed by immersion in 10% neutral-buffered formalin (Thermo
745 Fisher Scientific; 5705) for at least 2 days, before it was submitted to the SKCCC
746 Oncology Tissue and Imaging Service Core Laboratory (Johns Hopkins University, School
747 of Medicine) for downstream processing. The lungs were paraffin-embedded, 4 µm-
748 sectioned, and stained with hematoxylin and eosin (H&E). Slides were digitally scanned
749 at 40× using a Hamamatsu Nanozoomer S210 digital slide scanner (Hamamatsu
750 Photonics, Shizuoka, Japan) at 40X magnification (0.23 microns/pixel). Image files were
751 submitted in https://digital.pathology.johnshopkins.edu/ using Concentriq LS platform
752 (Proscia, PA, USA). Lung inflammation was quantified as a percentage of total lung area
753 using an in-house protocol developed with ImageJ software version 1.54m (NIH, USA) to
754 minimize human bias, through standardized software-based settings. Images were first

755 opened in ImageJ, and the scale was set by drawing a line over the scale bar using the
756 line tool and defining the known distance in millimeters under Analyze> Set Scale. Images
757 were then cropped to exclude the ruler (Image > Crop) and saved. For area quantification,
758 the Image> Adjust> Color Threshold tool was used, with consistent settings for hue (0–
759 255), saturation (0–255), and brightness (set based on analysis type)- full lung area=(0-
760 250) and inflamed area= (0-160). After selecting the ROI, the threshold window was
761 closed, and images were converted to binary format using Process> Binary> Make
762 Binary. The Signal to Noise ratio was improved by removing the Outliers- using Process>
763 Noise> Remove Outliers, adjusting the radius (=4) and the Threshold (=50).
764 Measurements were extracted (Analyze> Measure), with the initial setup requiring the
765 selection of "area" and "limit to threshold" under Set Measurements. Processed images
766 were saved, and the steps were repeated for all images with identical parameters to
767 ensure consistency. ROIs were then divided by the total lung area per slide to calculate
768 the ratio of inflamed to lung tissue- area.

769 **Multicolor Flow cytometry to quantify senescent cell population in *Mtb*-infected**
770 **mice lungs and spleen.**

771 To assess markers of senescence (p16+, p21+, and increased SA-βGalactosidase
772 activity) in lung and spleen tissues from *Mtb*-infected mice, organs were harvested at
773 indicated time points and dissociated using the Lung Dissociation Kit (Miltenyi Biotec;130-
774 095-927), and the gentleMACS Octo Dissociator (program m_lung_02), according to the
775 manufacturer's protocol. Single-cell suspensions were obtained by filtering dissociated
776 tissue through 70 µm mesh strainers (Corning; 431751), washing with 5 mL complete
777 RPMI media, and centrifuging at 300g for 5 min at RT. Red blood cells were lysed using

778 ACK lysis buffer (Quality Biological; 118156101), neutralized with complete RPMI, and
779 centrifuged. Cells were stained for viability using a live-dead near-IR dye (1:1000 dilution
780 in PBS; Thermo Fisher Scientific; L10119) and blocked with Rat Anti-Mouse CD16/CD32
781 Fc Block (Clone 2.4G2, BD Pharmingen; 553142). The panel of antibodies to detect the
782 senescent cell population (SenPanel) was designed using FluoroFinder
783 (https://fluorofinder.com/). For extracellular staining, cells were incubated with 50 µL of an
784 antibody cocktail in Brilliant Stain Buffer (BD Biosciences; 563794) containing anti- mouse
785 CD45 (Brilliant Violet 480; BD Biosciences;566095), CD11b (Brilliant Violet 650;
786 BioLegend; 101239), CD45R/B220 (Brilliant Violet 421; BioLegend; 103239), CD3
787 (StarBright Violet 610; BioRad-MCA500SBV610), EpCAM (PerCP-Cy5.5; BioLegend;
788 118220), F4/80 (PE-Dazzle 594; BioLegend; 123145), CD11c (PE-Fire 810; BioLegend;
789 161105), and Siglec-F (Alexa Fluor 700; BioLegend; 155533) for 30 minutes at 4°C in the
790 dark. After extracellular staining, cells were fixed with 4% formaldehyde, washed with
791 PBS, and incubated with the CellEvent™ Senescence Green Flow Cytometry Assay Kit
792 (Thermo Fisher Scientific; C10841; 1:250 dilution) in the senescence reaction buffer for 4
793 hours at 37°C, protected from light and without CO_2. Following incubation, cells were
794 washed and permeabilized using Perm/Wash buffer (BD Biosciences; 554723).
795 Intracellular staining was performed by incubating cells with a cocktail containing
796 p14ARF/CDKN2A Antibody (PE; Novus Biologicals; NB200-111PE), p21/CIP1/CDKN1A
797 Antibody (HJ21) (APC; Novus Biologicals; NBP2-47896APC), and CD68 (Brilliant Violet
798 785; BioLegend; 137035) for 60 minutes at 4°C in the dark. After staining, cells were
799 washed, filtered through strainer-capped BD FACS tubes (BD; 352235), and analyzed via
800 flow cytometry. 1×10^6 events per sample were acquired using a BD LSR Fortessa™ Cell

801 Analyzer (BD Biosciences), and the data were analyzed with FlowJo software version
802 10.8.1 (BD Biosciences). Single stain controls and compensation matrices were prepared
803 using UltraComp eBeads Plus Compensation Beads (Thermo Fisher Scientific; 01-3333-
804 41) and cells, as required. All flow antibodies were titrated to determine optimal staining
805 concentrations, and only manufacturer-validated antibodies with demonstrated specificity
806 were used. For the analysis, cells were first gated on singlets (FSC-H vs. FSC-A) and live
807 cells (live-dead near-IR negative) before further selection of cell types. T cells are
808 CD45+CD3+ and B cells are CD45+B220+. Myeloid cells: Tissue-resident Macrophages
809 are CD45+CD68+F4/80+CD11B-CD11C+, Interstitial macrophages are CD45+CD68+
810 F4/80+CD11B+CD11C+SiglecF-, Monocytes are CD45+CD68+F4/80+CD11B+CD11C-,
811 and Dendritic cells are CD45+CD68+F4/80-CD11B+CD11C+. Gating for $p16^+$, $p21^+$, and
812 SA-βGal^+ events for each cell type were established using reference cells from *Mtb*-
813 infected WT B6 mice (set at 1 %).

814 **Immunohistochemistry against p21 and γH2A.X (phosphor S139) in mice lungs.**

815 Immunostaining was conducted at the SKCCC Oncology Tissue and Imaging Service
816 Core Laboratory, Johns Hopkins University, School of Medicine. Immunolabeling for
817 γH2A.X (phospho S139) and p21 was performed on 4 µm-thick formalin-fixed, paraffin-
818 embedded (FFPE) tissue sections using the Ventana Discovery Ultra autostainer (Roche
819 Diagnostics). Sections underwent onboard dewaxing and rehydration, followed by
820 epitope retrieval in Ventana Ultra CC1 buffer (Roche Diagnostics; 6414575001) at 96°C
821 for 64 minutes. Primary antibodies- anti-gamma H2A.X (phospho S139) [EP854(2)Y]
822 (Abcam; ab81299; 1:1000 dilution) and Recombinant Anti-p21 antibody [EPR18021]
823 (Abcam; ab188224; 1:1000 dilution) were applied as indicated, at 36°C for 60 minutes.

824 Detection of the primary antibodies was achieved using the anti-rabbit HQ detection
825 system (Roche Diagnostics; Catalog 7017936001 and 7017812001), followed by
826 visualization with the Chromomap DAB IHC detection kit (Roche Diagnostics;
827 5266645001). Sections were counterstained with Mayer's hematoxylin, dehydrated, and
828 mounted. Whole-slide imaging was performed at the Oncology Tissue Services Core of
829 Johns Hopkins University using a Hamamatsu Nanozoomer S210 digital slide scanner
830 (Hamamatsu Photonics, Shizuoka, Japan) at 40X magnification (0.23 microns/pixel).
831 Images were visualized using the Concentriq digital pathology platform (Proscia,
832 Philadelphia, PA) and analyzed in ImageJ following a previously established in- house
833 protocol. Area quantification was performed using the Image> Adjust> Color Threshold
834 tool in ImageJ, applying consistent hue (0–255), saturation (0–255), and brightness
835 thresholds based on analysis type: full lung area (0–250) and DAB+ area (0–120).
836 Identical thresholds and detection settings were applied for all slides to ensure
837 consistency across analyses.

838 **Senescence-associated secretory phenotype (SASP)- cytokine quantification in**
839 ***Mtb*- infected mice lungs.**

840 To estimate SASP- cytokine levels, lung homogenates were centrifuged at 14,000 RPM
841 for 10 minutes at 4°C, and the resulting supernatants were filtered by a 0.2 µm filter, prior
842 to removal from the BSL3 facility. Supernatants were flash-frozen in liquid nitrogen and
843 stored at –80°C until cytokine quantification analysis. Cytokine levels in the lung
844 homogenate were measured using the LEGENDplex Mouse Inflammation Panel 13-plex
845 kit (BioLegend; 740446) following the manufacturer's protocol. Data acquisition was
846 performed on the CytoFLEX Flow Cytometer (Beckman Coulter), and cytokine

847 concentrations were analyzed using the LEGENDplex data analysis software Suite
848 (BioLegend). The amount of SASP cytokines were normalized to the protein
849 concentration of the homogenate (as measured by the BCA Assay kit).

850 **Drug preparation and study arms to test Senolytics as host- directed therapy *in***
851 ***vivo*.**

852 Dasatinib (Cayman Chemical; 11498), Fisetin (Cayman Chemical;15246), and Quercetin
853 (Millipore Sigma; Q4951) at required concentrations were first dissolved in 10ml DMSO
854 (Millipore Sigma; D2650) to make a stock solution. This mixture was then added to 190
855 ml of the Vehicle (60% Phosal 50 PG (Lipoid LLC; 368315), 30% PEG 400 (Sigma Aldrich;
856 202398), and 10% Ethanol) to prepare the final Senolytics reagent. Ethambutol (Millipore
857 Sigma; E4630) and Rifampicin (Millipore Sigma; R3501) were used as anti-*Mtb* drug
858 control. Solutions of Ethambutol and Rifampicin in distilled water were prepared and
859 stored at 4 °C.

860 After the day of aerosol infection, female mice were randomly divided into 4 groups (n = 4-
861 8 per group, as indicated in the Results). Feed and water were given *ad libitum*. Treatment
862 with drugs started at 2 weeks (*B6.Sst1S* mice and WT B6 Old), or 4 weeks (for WT B6
863 mice) post-infection. The drug treatment continued for another 6 weeks (for *B6.Sst1S*
864 mice), 3 weeks (for WT B6 Old) or 4 weeks (for WT B6). Treated mice were administered
865 Ethambutol (100 mg/kg of body weight) by oral gavage, once daily, 5 times a week.
866 Vehicle or Senolytics (Dasatinib: 5 mg/kg, Fisetin: 100 mg/kg, and Quercetin: 50 mg/kg
867 of body weight of mice) were administered by oral gavage, once daily, 3 times a week.
868 The fourth group received both the Ethambutol and Senolytics combination. All drugs
869 were administered in a total volume of 0.2 ml per treatment. Three infected mice were

870 sacrificed at the start of treatment as pretreatment controls. At indicated time points, mice
871 were sacrificed, and the lungs and spleen were harvested for the measurement of
872 bacterial burden, IHC, FACS and histopathology.

873 **Time to death assay.**

874 To examine if the Senolytics administration can improve the survival and body weight, the
875 survival of both male and female *B6.Sst1S* mice (8-10 weeks old) following *Mtb* infection
876 were assessed. Mice were infected via the aerosol route using a Glas-Col aerosolization
877 instrument to deliver a high dose of *Mtb* to the *B6.Sst1S* lungs (approximately 100 CFU).
878 After 3 weeks post-infection, infected mice were randomly divided into 4 groups and the
879 drug was administered as mentioned above, with slight modifications. The drug treatment
880 continued for another 4 weeks, where mice were administered Ethambutol (50 mg/kg of
881 body weight) by oral gavage, once daily, 5 times a week. In the second week, Ethambutol
882 (50 mg/kg of body weight) was combined with Rifampicin (10 mg/kg of body weight) for 1
883 week. Vehicle or Senolytics (Dasatinib: 5 mg/kg, Fisetin: 100 mg/kg, and Quercetin: 50
884 mg/kg of body weight of mice) were administered by oral gavage, once daily, 3 times a
885 week. The fourth group received both the Ethambutol and Senolytics combination. All
886 drugs were administered in a total volume of 0.2 ml per treatment. All mice were monitored
887 daily for signs of disease progression, including weight loss, lethargy, hunched posture,
888 and reduced activity. Survival data were analyzed using Kaplan-Meier survival curves to
889 determine the median time to death and assess differences between treatment groups.

890 **Statistical analysis.**

Statistical analyses were performed using GraphPad Prism version 10.4.0 software. Normality distribution was first assessed using the Shapiro-Wilk test. For comparisons of lung CFUs, data was $\log_{10}$-transformed and checked for normality before the analysis. Statistical significance was determined using unpaired two-tailed Student's t-tests or Mann Whitney test for two-group comparisons, and one-way or two- way ANOVA or Kruskal-Wallis test (non-parametric test) with post hoc tests for multiple- group comparisons. Kaplan-Meier survival analysis was conducted for time-to-death (TTD) studies, with group differences assessed by the Log-rank (Mantel-Cox) test. In animal experiments, each data point represented a single mouse, and experiments were randomized, though blinding was not implemented. Results are presented as mean with error bars indicating SEM. *p*-values less than 0.05 were considered statistically significant.

Contact for reagent and resource sharing.

All data associated with this study are present in the paper- either in the Results section or in the Supplementary files. Requests for further details on resources, protocol, and reagents can be directed to the corresponding author- Prof. William R Bishai. Raw data generated during this study is provided as a separate Excel file labeled "Source Data file". The RNA sequencing and Spatial transcriptomics datasets are available on NCBI's Gene Expression Omnibus (GEO). The *B6.Sst1S* mice used in this study are available for academic and non-commercial research upon request to Prof. Igor Kramnik, under a Material Transfer Agreement.

Acknowledgements

We gratefully acknowledge the support of the NIH grants AI152688, AI155602, CA006973, and R01HL126066 (to IK). We extend our gratitude to the SKCCC Core centers for their assistance with Histology and Flow cytometry. The funders have no role in study-design, data collection and interpretation, and the decision to submit the work for publication or preparation of the manuscript. We sincerely thank all the members of Prof. Bishai lab and Prof. Kramnik lab, for their valuable suggestions and discussions throughout this project. The schematic figures in this study were created using BioRender (with Academic Lab License).

Author contributions.

Funding Acquisition was contributed by- WB, IK. Conceptualization- WB, IK, SS. Methodology- WB, IK, SS, YMM, BK, SY, LK. Investigation and Formal Analysis- WB, IK, SS. Data curation and Validation- SS, SY, LK. Writing original draft- WB, IK, SS, SY. Review and editing manuscript- WB, IK, SS, YMM, BK, SY, LK.

Conflict of interest statement.

The authors declare that they have no competing or conflicting interests.

References

1. *2024 Global Tuberculosis Report*. https://www.who.int/teams/global-tuberculosis-programme/tb-reports/global-tuberculosis-report-2024.

2. Horton, K. C., Richards, A. S., Emery, J. C., Esmail, H. & Houben, R. M. G. J. Reevaluating progression and pathways following Mycobacterium tuberculosis infection within the spectrum of tuberculosis. *Proc Natl Acad Sci U S A* **120**, e2221186120 (2023).

3. Sossen, B. *et al.* The natural history of untreated pulmonary tuberculosis in adults: a systematic review and meta-analysis. *Lancet Respir Med* **11**, 367–379 (2023).

4. Richards, A. S. *et al.* Quantifying progression and regression across the spectrum of pulmonary tuberculosis: a data synthesis study. *Lancet Glob Health* **11**, e684–e692 (2023).

5. Nguyen, H. V., Tiemersma, E., Nguyen, N. V., Nguyen, H. B. & Cobelens, F. Disease Transmission by Patients With Subclinical Tuberculosis. *Clin Infect Dis* **76**, 2000–2006 (2023).

6. Chen, R. Y. *et al.* Radiological and functional evidence of the bronchial spread of tuberculosis: an observational analysis. *Lancet Microbe* **2**, e518–e526 (2021).

7. GBD Tuberculosis Collaborators. The global burden of tuberculosis: results from the Global Burden of Disease Study 2015. *Lancet Infect Dis* **18**, 261–284 (2018).

8. Olmo-Fontánez, A. M. & Turner, J. Tuberculosis in an Aging World. *Pathogens* **11**, (2022).

9. Negin, J., Abimbola, S. & Marais, B. J. Tuberculosis among older adults--time to take notice. *Int J Infect Dis* **32**, 135–7 (2015).

10. Caraux-Paz, P., Diamantis, S., de Wazières, B. & Gallien, S. Tuberculosis in the Elderly. *J Clin Med* **10**, 5888 (2021).

11. Teo, A. K. J. *et al.* Tuberculosis in older adults: challenges and best practices in the Western Pacific Region. *Lancet Reg Health West Pac* **36**, 100770 (2023).

12. Orme, I. M. Aging and immunity to tuberculosis: prolonged survival of old mice infected with Mycobacterium tuberculosis by adoptive immunization with memory-immune T lymphocytes. *Cell Immunol* **118**, 229–33 (1989).

13. Orme, I. M. A mouse model of the recrudescence of latent tuberculosis in the elderly. *Am Rev Respir Dis* **137**, 716–8 (1988).

14. Turner, J., Frank, A. A. & Orme, I. M. Old mice express a transient early resistance to pulmonary tuberculosis that is mediated by CD8 T cells. *Infect Immun* **70**, 4628–37 (2002).

969 15. Torrelles, J. B. *et al.* The Impact of Aging on the Lung Alveolar Environment,
970 Predetermining Susceptibility to Respiratory Infections. *Frontiers in Aging* **3**, 1–9
971 (2022).

972 16. Canan, C. H. *et al.* Characterization of lung inflammation and its impact on
973 macrophage function in aging. *J Leukoc Biol* **96**, 473–480 (2014).

974 17. Lafuse, W. P. *et al.* Identification of an Increased Alveolar Macrophage
975 Subpopulation in Old Mice That Displays Unique Inflammatory Characteristics and
976 Is Permissive to Mycobacterium tuberculosis Infection. *J Immunol* **203**, 2252–
977 2264 (2019).

978 18. Olmo-Fontánez, A. M. *et al.* Impact of the elderly lung mucosa on Mycobacterium
979 tuberculosis transcriptional adaptation during infection of alveolar epithelial cells.
980 *Microbiol Spectr* **12**, e0179024 (2024).

981 19. Olmo-Fontánez, A. M. *et al.* Human alveolar lining fluid from the elderly promotes
982 Mycobacterium tuberculosis intracellular growth and translocation into the cytosol
983 of alveolar epithelial cells. *Mucosal Immunol* **17**, 155–168 (2024).

984 20. Moliva, J. I. *et al.* The Lung Mucosa Environment in the Elderly Increases Host
985 Susceptibility to Mycobacterium tuberculosis Infection. *Journal of Infectious*
986 *Diseases* **220**, 514–523 (2019).

987 21. Di Micco, R., Krizhanovsky, V., Baker, D. & d'Adda di Fagagna, F. Cellular
988 senescence in ageing: from mechanisms to therapeutic opportunities. *Nat Rev*
989 *Mol Cell Biol* **22**, 75–95 (2021).

990 22. Wissler Gerdes, E. O., Zhu, Y., Tchkonia, T. & Kirkland, J. L. Discovery,
991 development, and future application of senolytics: theories and predictions. *FEBS*
992 *J* **287**, 2418–2427 (2020).

993 23. Kennedy, B. K. *et al.* Geroscience: linking aging to chronic disease. *Cell* **159**,
994 709–13 (2014).

995 24. Wang, B., Han, J., Elisseeff, J. H. & Demaria, M. The senescence-associated
996 secretory phenotype and its physiological and pathological implications. *Nat Rev*
997 *Mol Cell Biol* **25**, 958–978 (2024).

998 25. Salminen, A., Kauppinen, A. & Kaarniranta, K. Myeloid-derived suppressor cells
999 (MDSC): an important partner in cellular/tissue senescence. *Biogerontology* **19**,
1000 325–339 (2018).

1001 26. Ruhland, M. K. *et al.* Stromal senescence establishes an immunosuppressive
1002 microenvironment that drives tumorigenesis. *Nat Commun* **7**, 11762 (2016).

1003 27. Salminen, A. Immunosuppressive network promotes immunosenescence
1004 associated with aging and chronic inflammatory conditions. *J Mol Med (Berl)* **99**,
1005 1553–1569 (2021).

1006 28. Xu, M. *et al.* Transplanted Senescent Cells Induce an Osteoarthritis-Like
1007 Condition in Mice. *J Gerontol A Biol Sci Med Sci* **72**, 780–785 (2017).

1008 29. Franco, A. C. *et al.* Senescent cell transplantation into the skin induces age-
1009 related peripheral dysfunction and cognitive decline. *Aging Cell* **24**, (2025).

1010 30. Childs, B. G., Durik, M., Baker, D. J. & van Deursen, J. M. Cellular senescence in
1011 aging and age-related disease: from mechanisms to therapy. *Nat Med* **21**, 1424–
1012 35 (2015).

1013 31. Justice, J. N. *et al.* Senolytics in idiopathic pulmonary fibrosis: Results from a first-
1014 in-human, open-label, pilot study. *EBioMedicine* **40**, 554–563 (2019).

1015 32. Pichugin, A. V., Yan, B. S., Sloutsky, A., Kobzik, L. & Kramnik, I. Dominant role of
1016 the sst1 locus in pathogenesis of necrotizing lung granulomas during chronic
1017 tuberculosis infection and reactivation in genetically resistant hosts. *American*
1018 *Journal of Pathology* **174**, 2190–2201 (2009).

1019 33. Yan, B. S., Kirby, A., Shebzukhov, Y. V., Daly, M. J. & Kramnik, I. Genetic
1020 architecture of tuberculosis resistance in a mouse model of infection. *Genes*
1021 *Immun* **7**, 201–210 (2006).

1022 34. Ji, D. X. *et al.* Type I interferon-driven susceptibility to Mycobacterium tuberculosis
1023 is mediated by IL-1Ra. *Nat Microbiol* **4**, 2128–2135 (2019).

1024 35. Yabaji, S. M. *et al.* Cell state transition analysis identifies interventions that
1025 improve control of Mycobacterium tuberculosis infection by susceptible
1026 macrophages. *Sci Adv* **9**, eadh4119 (2023).

1027 36. Pan, H. *et al.* Ipr1 gene mediates innate immunity to tuberculosis. *Nature* **434**,
1028 767–772 (2005).

1029 37. Krug, S. *et al.* Adjunctive Integrated Stress Response Inhibition Accelerates
1030 Tuberculosis Clearance in Mice. *mBio* **14**, e0349622 (2023).

1031 38. Bhattacharya, B. *et al.* The integrated stress response mediates necrosis in
1032 murine Mycobacterium tuberculosis granulomas. *Journal of Clinical Investigation*
1033 **131**, (2021).

1034 39. Fraschilla, I., Amatullah, H., Rahman, R. U. & Jeffrey, K. L. Immune chromatin
1035 reader SP140 regulates microbiota and risk for inflammatory bowel disease. *Cell*
1036 *Host Microbe* **30**, 1370-1381.e5 (2022).

1037 40. Ji, D. X. *et al.* Role of the transcriptional regulator SP140 in resistance to bacterial
1038 infections via repression of type I interferons. *Elife* **10**, (2021).

1039 41. Yabaji, S. M. *et al.* Lipid Peroxidation and Type I Interferon Coupling Fuels
1040 Pathogenic Macrophage Activation Causing Tuberculosis Susceptibility. *bioRxiv*
1041 (2024) doi:10.1101/2024.03.05.583602.

1042 42. Moreira-Teixeira, L. *et al.* Type I IFN exacerbates disease in tuberculosis-
1043 susceptible mice by inducing neutrophil-mediated lung inflammation and NETosis.
1044 *Nat Commun* **11**, 5566 (2020).

1045 43. Berry, M. P. R. *et al.* An interferon-inducible neutrophil-driven blood transcriptional
1046 signature in human tuberculosis. *Nature* **466**, 973–7 (2010).

1047 44. Kotov, D. I. *et al.* Early cellular mechanisms of type I interferon-driven
1048 susceptibility to tuberculosis. *Cell* **186**, 5536-5553.e22 (2023).

1049 45. Zhou, Y. *et al.* Metascape provides a biologist-oriented resource for the analysis of
1050 systems-level datasets. *Nat Commun* **10**, 1523 (2019).

1051 46. Kalinin, A., Zubkova, E. & Menshikov, M. Integrated Stress Response (ISR)
1052 Pathway: Unraveling Its Role in Cellular Senescence. *Int J Mol Sci* **24**, (2023).

1053 47. Payea, M. J. *et al.* Senescence suppresses the integrated stress response and
1054 activates a stress-remodeled secretory phenotype. *Mol Cell* **84**, 4454-4469.e7
1055 (2024).

1056 48. Katlinskaya, Y. V *et al.* Suppression of Type I Interferon Signaling Overcomes
1057 Oncogene-Induced Senescence and Mediates Melanoma Development and
1058 Progression. *Cell Rep* **15**, 171–180 (2016).

1059 49. De Cecco, M. *et al.* L1 drives IFN in senescent cells and promotes age-
1060 associated inflammation. *Nature* **566**, 73–78 (2019).

1061 50. Kandhaya-Pillai, R. *et al.* TNFα-senescence initiates a STAT-dependent positive
1062 feedback loop, leading to a sustained interferon signature, DNA damage, and
1063 cytokine secretion. *Aging* **9**, 2411–2435 (2017).

1064 51. Paramos-de-Carvalho, D., Jacinto, A. & Saúde, L. The right time for senescence.
1065 *Elife* **10**, 1–21 (2021).

1066 52. Lionaki, E. & Tavernarakis, N. Cell Senescence: Methods and Protocols, Methods
1067 in Molecular Biology. *Cell Senescence* **965**, 473–484 (2013).

1068 53. Sharpless, N. E. & Sherr, C. J. Forging a signature of in vivo senescence. *Nat*
1069 *Rev Cancer* **15**, 397–408 (2015).

1070 54. Hernandez-Segura, A., Nehme, J. & Demaria, M. Hallmarks of Cellular
1071 Senescence. *Trends Cell Biol* **28**, 436–453 (2018).

1072 55. Yabaji, S. M. *et al.* Protocol for Developing a Mouse Model of Post Primary
1073 Pulmonary Tuberculosis after Hematogenous Spread in Native Lungs and Lung
1074 Implants. *bioRxiv* 2025.02.28.640830 (2025) doi:10.1101/2025.02.28.640830.

1075 56. Saul, D. *et al.* A new gene set identifies senescent cells and predicts senescence-
1076 associated pathways across tissues. *Nat Commun* **13**, (2022).

1077 57. González-Gualda, E., Baker, A. G., Fruk, L. & Muñoz-Espín, D. A guide to
1078 assessing cellular senescence in vitro and in vivo. *FEBS Journal* **288**, 56–80
1079 (2021).

1080 58. Zhang, L. *et al.* Cellular senescence: a key therapeutic target in aging and
1081 diseases. *J Clin Invest* **132**, (2022).

1082 59. Suda, M. *et al.* Senolytic vaccination improves normal and pathological age-
1083 related phenotypes and increases lifespan in progeroid mice. *Nat Aging* **1**, 1117–
1084 1126 (2021).

1085 60. Zhu, Y. *et al.* The Achilles' heel of senescent cells: from transcriptome to senolytic
1086 drugs. *Aging Cell* **14**, 644–58 (2015).

1087 61. Raffaele, M. & Vinciguerra, M. The costs and benefits of senotherapeutics for
1088 human health. *Lancet Healthy Longev* **3**, e67–e77 (2022).

1089 62. Robbins, P. D. *et al.* Senolytic Drugs: Reducing Senescent Cell Viability to Extend
1090 Health Span. *Annu Rev Pharmacol Toxicol* **61**, 779–803 (2021).

1091 63. Chaib, S., Tchkonia, T. & Kirkland, J. L. Cellular senescence and senolytics: the
1092 path to the clinic. *Nat Med* **28**, 1556–1568 (2022).

1093 64. Lee, E. *et al.* Exploring the effects of Dasatinib, Quercetin, and Fisetin on DNA
1094 methylation clocks: a longitudinal study on senolytic interventions. *Aging* **16**,
1095 3088–3106 (2024).

1096 65. Shah, N. P. *et al.* Overriding imatinib resistance with a novel ABL kinase inhibitor.
1097 *Science* **305**, 399–401 (2004).

1098 66. Yousefzadeh, M. J. *et al.* Fisetin is a senotherapeutic that extends health and
1099 lifespan. *EBioMedicine* **36**, 18–28 (2018).

1100 67. Zhu, Y. *et al.* New agents that target senescent cells: the flavone, fisetin, and the
1101 BCL-XL inhibitors, A1331852 and A1155463. *Aging* **9**, 955–963 (2017).

1102 68. Lim, J. Y., Lee, J. Y., Byun, B. J. & Kim, S. H. Fisetin targets phosphatidylinositol-
1103 3-kinase and induces apoptosis of human B lymphoma Raji cells. *Toxicol Rep* **2**,
1104 984–989 (2015).

1105 69. Kim, J. A. *et al.* Fisetin, a dietary flavonoid, induces apoptosis of cancer cells by
1106 inhibiting HSF1 activity through blocking its binding to the hsp70 promoter.
1107 *Carcinogenesis* **36**, 696–706 (2015).

1108 70. Amaral, E. P. *et al.* BACH1 promotes tissue necrosis and Mycobacterium
1109 tuberculosis susceptibility. *Nat Microbiol* **9**, 120–135 (2024).

1110 71. Orme, I. Mechanisms underlying the increased susceptibility of aged mice to
1111 tuberculosis. *Nutr Rev* **53**, S35-8; discussion S38-40 (1995).

1112 72. Vesosky, B. & Turner, J. The influence of age on immunity to infection with
1113 Mycobacterium tuberculosis. *Immunol Rev* **205**, 229–43 (2005).

1114 73. Rottinghaus, E. K., Vesosky, B. & Turner, J. TLR-2 independent recognition of
1115 Mycobacterium tuberculosis by CD11c+ pulmonary cells from old mice. *Mech*
1116 *Ageing Dev* **131**, 405–14 (2010).

1117 74. Bobak, C. A. *et al.* Increased DNA methylation, cellular senescence and
1118 premature epigenetic aging in guinea pigs and humans with tuberculosis. *Aging*
1119 **14**, 2174–2193 (2022).

1120 75. DiNardo, A. R. *et al.* DNA hypermethylation during tuberculosis dampens host
1121 immune responsiveness. *J Clin Invest* **130**, 3113–3123 (2020).

1122 76. Udomsinprasert, W. *et al.* Leukocyte telomere length as a diagnostic biomarker
1123 for anti-tuberculosis drug-induced liver injury. *Sci Rep* **10**, (2020).

1124 77. Freimane, L. *et al.* Telomere length and mitochondrial DNA copy number in
1125 multidrug-resistant tuberculosis. *Tuberculosis* **131**, (2021).

1126 78. Katoto, P. D. M. C. *et al.* Telomere length and outcome of treatment for pulmonary
1127 tuberculosis in a gold mining community. *Sci Rep* **11**, (2021).

1128 79. Lochab, S., Singh, Y., Sengupta, S. & Nandicoori, V. K. Mycobacterium
1129 tuberculosis exploits host ATM kinase for survival advantage through secA2
1130 secretome. *Elife* **9**, (2020).

1131 80. Cumming, B. M., Addicott, K. W., Adamson, J. H. & Steyn, A. J. C. Mycobacterium
1132 tuberculosis induces decelerated bioenergetic metabolism in human
1133 macrophages. *Elife* **7**, 1–28 (2018).

1134 81. Cumming, B. M. *et al.* Mycobacterium tuberculosis arrests host cycle at the G1/S
1135 transition to establish long term infection. *PLoS Pathog* **13**, (2017).

1136 82. Cyktor, J. C. *et al.* Killer cell lectin-like receptor G1 deficiency significantly
1137 enhances survival after Mycobacterium tuberculosis infection. *Infect Immun* **81**,
1138 1090–9 (2013).

1139 83. Chang, E., Cavallo, K. & Behar, S. M. CD4 T cell dysfunction is associated with
1140 bacterial recrudescence during chronic tuberculosis. *Nat Commun* **16**, 2636
1141 (2025).

1142 84. Chien, Y. *et al.* Control of the senescence-associated secretory phenotype by NF-
1143 κB promotes senescence and enhances chemosensitivity. *Genes Dev* **25**, 2125–
1144 36 (2011).

1145 85. Miwa, S., Kashyap, S., Chini, E. & von Zglinicki, T. Mitochondrial dysfunction in
1146 cell senescence and aging. *J Clin Invest* **132**, (2022).

1147 86. Flores, R. R. *et al.* Expansion of myeloid-derived suppressor cells with aging in
1148 the bone marrow of mice through a NF-κB-dependent mechanism. *Aging Cell* **16**,
1149 480–487 (2017).

1150 87. Shi, H., Li, K., Ni, Y., Liang, X. & Zhao, X. Myeloid-Derived Suppressor Cells:
1151 Implications in the Resistance of Malignant Tumors to T Cell-Based
1152 Immunotherapy. *Front Cell Dev Biol* **9**, 707198 (2021).

1153 88. Ostrand-Rosenberg, S. Myeloid derived-suppressor cells: their role in cancer and
1154 obesity. *Curr Opin Immunol* **51**, 68–75 (2018).

1155 89. Umansky, V., Blattner, C., Gebhardt, C. & Utikal, J. The Role of Myeloid-Derived
1156 Suppressor Cells (MDSC) in Cancer Progression. *Vaccines (Basel)* **4**, 36 (2016).

1157 90. VanValkenburg, A. *et al.* Malnutrition leads to increased inflammation and
1158 expression of tuberculosis risk signatures in recently exposed household contacts
1159 of pulmonary tuberculosis. *Front Immunol* **13**, 1011166 (2022).

1160 91. Cottage, C. T. *et al.* Targeting p16-induced senescence prevents cigarette smoke-
1161 induced emphysema by promoting IGF1/Akt1 signaling in mice. *Commun Biol* **2**,
1162 307 (2019).

1163 92. Marino, F. *et al.* Diabetes-Induced Cellular Senescence and Senescence-
1164 Associated Secretory Phenotype Impair Cardiac Regeneration and Function
1165 Independently of Age. *Diabetes* **71**, 1081–1098 (2022).

1166 93. Topiwala, A. *et al.* Alcohol consumption and telomere length: Mendelian
1167 randomization clarifies alcohol's effects. *Mol Psychiatry* **27**, 4001–4008 (2022).

1168 94. Restrepo, B. I. *et al.* Differential Role of Type 2 Diabetes as a Risk Factor for
1169 Tuberculosis in the Elderly versus Younger Adults. *Pathogens* **11**, 1551 (2022).

1170 95. Auld, E. *et al.* HIV Infection Is Associated with Shortened Telomere Length in
1171 Ugandans with Suspected Tuberculosis. *PLoS One* **11**, e0163153 (2016).

1172 96. Auld, S. C. *et al.* Pathogenesis of Post-Tuberculosis Lung Disease: Defining
1173 Knowledge Gaps and Research Priorities at the Second International Post-
1174 Tuberculosis Symposium. *Am J Respir Crit Care Med* **210**, 979–993 (2024).

1175 97. Ravimohan, S., Kornfeld, H., Weissman, D. & Bisson, G. P. Tuberculosis and lung
1176 damage: from epidemiology to pathophysiology. *Eur Respir Rev* **27**, (2018).

1177 98. Auld, S. C. *et al.* Pulmonary restriction predicts long-term pulmonary impairment
1178 in people with HIV and tuberculosis. *BMC Pulm Med* **21**, 19 (2021).

1179 99. Allwood, B. W. *et al.* Perspectives from the 2nd International Post-Tuberculosis
1180 Symposium: mobilising advocacy and research for improved outcomes. *IJTLD*
1181 *open* **1**, 111–123 (2024).

1182 100. Schafer, M. J. *et al.* Cellular senescence mediates fibrotic pulmonary disease. *Nat*
1183 *Commun* **8**, 14532 (2017).

1184 101. Parveen, S. *et al.* Glutamine metabolism inhibition has dual immunomodulatory
1185 and antibacterial activities against Mycobacterium tuberculosis. *Nat Commun* **14**,
1186 7427 (2023).

1187 102. Love, M. I., Huber, W. & Anders, S. Moderated estimation of fold change and
1188 dispersion for RNA-seq data with DESeq2. *Genome Biol* **15**, 1–21 (2014).

1189 103. Shee, S. *et al.* Moxifloxacin-Mediated Killing of Mycobacterium tuberculosis
1190 Involves Respiratory Downshift, Reductive Stress, and Accumulation of Reactive
1191 Oxygen Species. *Antimicrob Agents Chemother* **66**, (2022).

1192 104. Merritt, C. R. *et al.* Multiplex digital spatial profiling of proteins and RNA in fixed
1193 tissue. *Nat Biotechnol* **38**, 586–599 (2020).

1194 105. Danaher, P. *et al.* Advances in mixed cell deconvolution enable quantification of
1195 cell types in spatial transcriptomic data. *Nat Commun* **13**, 385 (2022).

1196 106. Krug, S. *et al.* Inhibition of host PARP1 contributes to the anti-inflammatory and
1197 antitubercular activity of pyrazinamide. *Nat Commun* **14**, 8161 (2023).

1198

1199

1200 **Figure legends.**

1201 **Figure 1. Evidence of senescence-like phenotype in uninfected BMDMs derived**
1202 **from young *B6. Sst1S* and WT B6 Old mice**. (A) Schematic to determine senescence
1203 associated markers in BMDMs. (B) Median Fluorescence intensity of fluorescent SA-βGal
1204 substrate by live BMDMs in presence or absence of TNFα for 48 h. 10 μM Etoposide
1205 treated WT B6 BMDMs or BMDMs from aged mice are used as positive control. (C,D)
1206 quantification and representative images of SA-βGal- positive BMDMs (PFA-fixed)
1207 located at the center of the TC-treated well at 20X magnification by bright field
1208 microscopy. (E) mRNA levels of SASP- associated genes normalized to ActB as
1209 determined by qPCR. (F) BrdU incorporation by BMDMs in absence or presence of TNFα,
1210 respectively with time. (G) BMDMs were infected for 4 hours with *Mtb* H37Rv at MOI=10,
1211 followed by removal of extracellular bacteria by extensive washing with warm media.
1212 Intramacrophage survival was determined by enumerating CFU at 2 days post-infection.
1213 The data are means ± SEM. Data is representative of two independent experiments done
1214 with n≥2. (p>0.05: ns, p<0.05: *, p<0.01: **, p<0.001: ***, p<0.0001: ****, one-way ANOVA
1215 with Tukey's (B, C, F, G) or two-way ANOVA with Sidak's (E) multiple comparisons test).

1216

1217 **Figure 2. Detection of Senescence-associated markers during early stages of**
1218 **disease progression in *Mtb* infected mice.** (A) Schematics of Spatial transcriptomics
1219 using a Nanostring GeoMX Digital Spatial Profiler to determine differential gene
1220 expression in cells at non-controlling multibacillary granulomatous lesions (*NC*) relative
1221 to controlling lesions (*C*) in *B6.Sst1S* mice lungs. (n= 8 ROI). (B) Volcano plot to show
1222 differentially expressed genes between controlling and non-controlling granulomatous

1223 lesions. Significantly upregulated (fold change> 2) and downregulated (fold change< 2)
1224 genes (*p.adj*< 0.05) in *NC* relative to *C* granulomas are shown in red and cyan,
1225 respectively. Top senescence associated genes in upregulated DEGs are labelled. (C)
1226 Schematics of the experimental strategy to measure senescence markers *in vivo* at 2-
1227 and 4-weeks post infection. Day1 CFU=39. *Mtb* H37Rv burden at indicated time points in
1228 WT B6, *B6.Sst1S* and WT B6 old mice (D) lungs and (E) spleen. The data are means ±
1229 SEM. *p* was determined by two-way ANOVA with Tukey's multiple comparisons test
1230 (*p*>0.05: ns, *p*<0.05: *, *p*<0.0001: ****). Representative H&E-stained and
1231 Immunohistochemistry against γH2A.X and p21 of mice lungs at (F) 2 weeks p.i. (arrow
1232 indicates no difference in *Mtb* burden) and (G) 4 weeks p.i. (H) ImageJ quantification of
1233 lung pathology (H&E-stained area) in uninfected mice and *Mtb* H37Rv infected mice lungs
1234 at 2 weeks and 4 weeks p.i. (n=4-6). Squares indicate necrotic granulomas. (I) ImageJ
1235 quantification of γH2A.X-stained area in uninfected mice and *Mtb* H37Rv infected mice
1236 lungs, and (J) corresponding γH2A.X-IHC intensity at 2 weeks and 4 weeks p.i. (n=4-6
1237 mice/group). The data are means ± SEM. Each data point represents a mouse. Statistical
1238 analysis between two groups was measured by unpaired two- tailed Student's t test
1239 (normal distribution) or Mann Whitney test.

1240

1241 **Figure 3. Detection of senescent cell population and SASP cytokines by flow**
1242 **cytometry during early stages of disease progression in *Mtb*-infected mice.** (A)
1243 Schematics of the experimental strategy to measure senescence markers (p21, p16 and
1244 SA- βGal activity) and SASP cytokines levels in mice lungs at 10 and 20 days p.i. Young
1245 WT B6, *B6.Sst1S*, and old WT B6 mice were aerosol-infected with 55 CFU of *Mtb* H37Rv.

1246 *Mtb* H37Rv burden in mice (B) lungs and (C) spleen are shown at indicated time points
1247 (n= 6-9 mice/ group). The data are means ± SEM. Each data point represents a mouse.
1248 Statistical analysis was calculated by two-way (B) or one- way (C) ANOVA with Tukey's
1249 multiple comparisons test. (p>0.05: ns, p<0.0001: ****). (D) %p21+p16+ and (E) %SA-
1250 βGal+ (CellEvent Senescence green+) cells out of all live lung (uninfected and *Mtb*-
1251 infected mice) and Spleen (*Mtb*-infected mice) cells at 10 days p.i. as determined by
1252 multicolor flow cytometry. (F) %p21+p16+ and (G) %SA-βGal+ cells out of different lung-
1253 cell types at 10 days p.i., as determined by multicolor flow cytometry. Gating for $p16^+$,
1254 $p21^+$, and SA-$βGal^+$ events for each cell type were established using Fluorescence minus
1255 one (FMO) controls and reference cells from *Mtb*-infected WT B6 mice (set at 1%). (AMs:
1256 Alveolar macrophages, IMs: Interstitial macrophages) **(H)** Normalized concentration of
1257 SASP- cytokines in lung homogenates at 20 dpi and 4 wpi relative to WT B6 mice as
1258 measured by a LEGENDplex™ Mouse Inflammation Panel. The data are means ± SEM.
1259 Each data point represents a mouse (n=11-12). (two-way ANOVA with Tukey's (D-G) or
1260 Dunnett's (H) multiple comparisons test).

1261

1262 **Figure 4. Global transcriptomics data by RNA Sequencing revealed upregulation of**
1263 **pro-survival pathways- PI3K-ERK1/2 and MAPK cascade in BMDMs derived from**
1264 **young *B6.Sst1S.*** (A) Schematic of the experiment. (B) Selective representation of Gene-
1265 Ontology (GO) analysis for the differentially expressed genes indicating all enriched
1266 ($p.adj$< 0.05) signaling pathways under TNFα, *Mtb* and TNFα+ *Mtb*- treatment conditions.
1267 The size of the bubble indicates $p.adj$ values relative to similarly treated WT B6, and color
1268 indicates the percentage of DEGs out of total genes in that GO class. (C) Volcano plot of

1269 DEGs (=1177) with upregulated genes in TNFα+ *Mtb- treated B6.Sst1S* BMDMs (log2
1270 fold change >1; *p. adj.*< 0.05) shown in light gray and downregulated genes (log2 fold
1271 change <1; *p. adj.*< 0.05) shown in light pink, relative to stressed WT B6 BMDMs. Genes
1272 representative of top significantly enriched GO class- Receptor tyrosine kinase signaling/
1273 PI3K pathway (shown in orange), MAPK cascade (blue), anti-apoptotic genes (red) and
1274 SenMayo gene set (pink) are shown. Top expected downregulated genes- Sp140, Sp110
1275 and Erdr1 are shown in yellow.
1276
1277 **Figure 5. Senolytics DQF administration with or without anti-TB drug improved**
1278 **survival, body weight and reduced *Mtb* burden in mice**. (A) Both male and female
1279 *B6.Sst1S* mice were aerosol infected with high-dose 91 CFU of *Mtb* H37Rv and at 3
1280 weeks p.i., mice were oral gavaged with vehicle (n=16 mice)/ drugs (n=11 mice) for the
1281 next 4 weeks. (B) At 3 weeks p.i., the *Mtb* burden in lungs and spleen were $1.5*10^7$ and
1282 $1.6*10^5$ CFU, respectively. (circles indicate females and squares indicate males, n=4-5
1283 mice). Mice were monitored for changes in body weight and survival after the start of drug
1284 treatment. (C) Kaplan-Meir survival curve of *B6.Sst1S* mice. Line indicates duration of
1285 therapy. Indicated *p* values are measured by log-rank (Mantel-Cox) test. (D) Changes in
1286 body weight are plotted as a % change in body weight of surviving mice relative to Day 1
1287 p.i. over time. The data are means ± SEM. (p<0.05: *, two-way ANOVA with Tukey's
1288 multiple comparisons test). (E) The experimental strategy. Day 1 CFU in *B6.Sst1S* mice=
1289 11 (low dose); WT B6 young and old mice= 126. *Mtb* H37Rv burden in (F) lung and (G)
1290 spleen of WT B6, *B6.Sst1S* and old WT B6 mice at indicated time points (n=4-7). Square
1291 indicates CFU below the limit of detection (=10 CFU). The green arrow indicates the start

1292 of drug treatment. The data are means ± SEM. Each data point represents a mouse. n=
1293 4-7 mice/ group. Statistical analysis was done by one-way ANOVA with Sidak's multiple
1294 comparison test or Kruskal-Wallis Dunn's multiple comparison test (5G-WT B6).

1295

1296 **Figure 6. Senolytics administration alone, and in combination with Ethambutol**
1297 **reduced lung pathology and senescence- associated marker in *Mtb* H37Rv infected**
1298 ***B6.Sst1S* and WT B6 old mice.** (A) Representative H&E-stained images of *Mtb*- infected
1299 mice lungs treated with Vehicle or drugs, and respective ImageJ- based quantification.
1300 Yellow arrow indicates necrotic granuloma in Vehicle treated *B6.Sst1S* mice at 5 wpi. The
1301 number in parenthesis indicate the number of mice with necrotic granuloma at 5 wpi. (B)
1302 Representative γH2A.X- Immunohistochemistry images of mice after lungs vehicle/ drugs
1303 treatment, and respective Violin plots to show ImageJ quantification of γH2A.X-stained
1304 area and (C) γH2A.X- stain intensity at indicated time points. Each data point represents
1305 a mouse. n=4-7 mice/group. Statistical analysis between two groups was done by
1306 unpaired two- tailed Student's t test or Mann-Whitney test.

1307

1308 **Figure 7. Senolytics administration alone, and in combination with Ethambutol**
1309 **reduced p21+SA-βGal+ or p16+SA-βGal+ senescent population in *Mtb* H37Rv**
1310 **infected *B6.Sst1S* and WT B6 old mice.** %p21+βGal+ and %p16+βGal+ subpopulation
1311 observed in all live lung cells of Mtb- infected (A) *B6.Sst1S* (B) WT B6 old, and (C) young
1312 WT B6 mice (n= 5-8),. The data are means ± SEM. Each data point represents a mouse.
1313 Statistical analysis was calculated by two-way ANOVA with Dunnett's multiple
1314 comparisons test. Bubble plot to show %p21+βGal+ and %p16+βGal+ subpopulation in

1315 different lung cell types in *Mtb*-infected (D) *B6.Sst1S* mice (n= 8) and (E) WT B6 old mice
1316 (n= 5) at indicated timepoint and treatment groups. The size of the bubble indicates
1317 %subpopulation out of all of particular cell types and color is adjusted *p* values relative to
1318 the Veh group. Statistics are calculated by one-way ANOVA with Tukey's multiple
1319 comparisons test. (F) Proposed model showing the crosstalk between senescence and
1320 necrotic granuloma trajectory.

1321

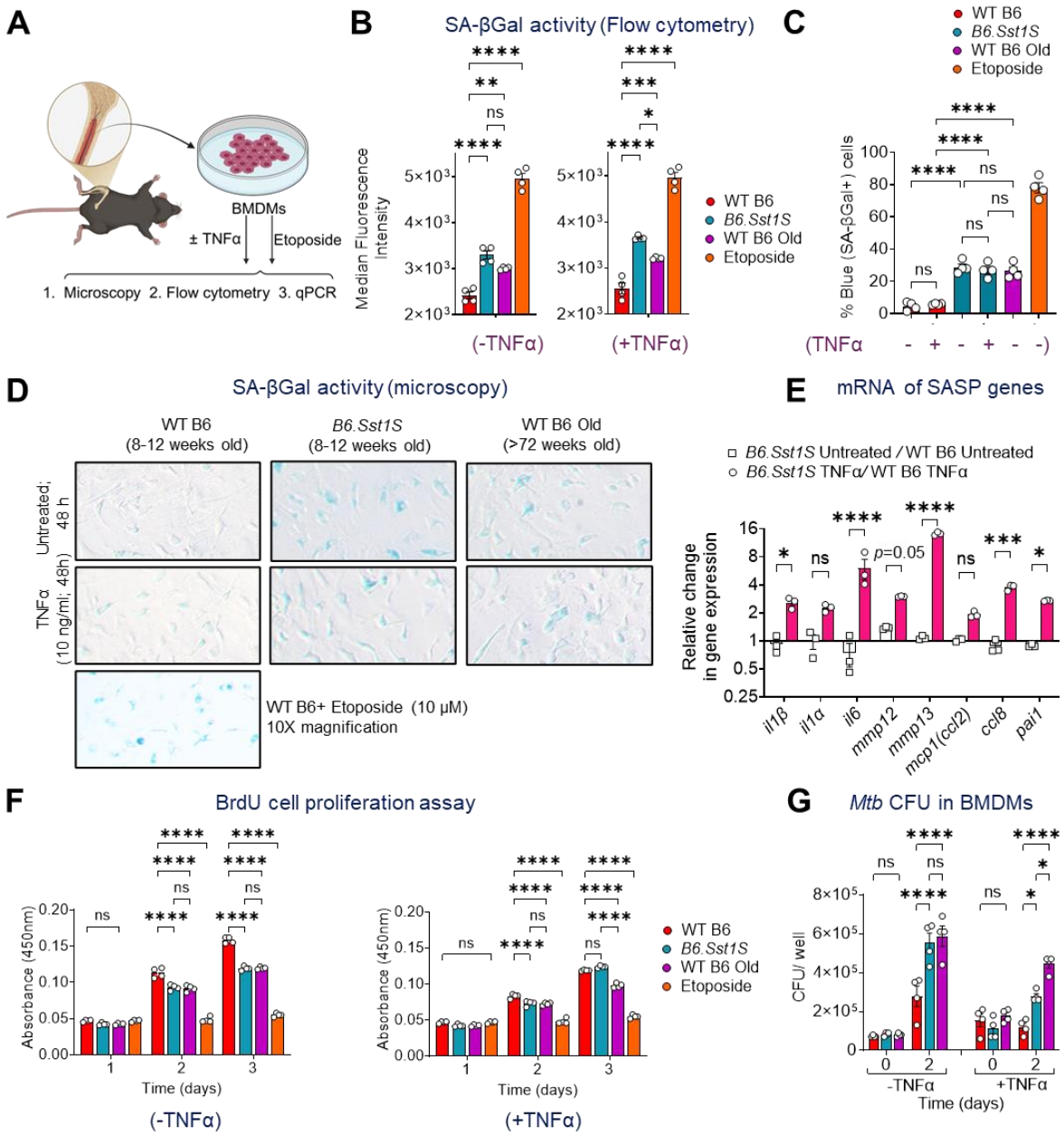

Figure 1. Evidence of senescence-like phenotype in uninfected BMDMs derived from young *B6. Sst1S* and WT B6 Old mice. (A) Schematic to determine senescence associated markers in BMDMs. (B) Median Fluorescence intensity of fluorescent SA-βGal substrate by live BMDMs in presence or absence of TNFα for 48 h. 10 μM Etoposide treated WT B6 BMDMs or BMDMs from aged mice are used as positive control. (C,D) quantification and representative images of SA-βGal- positive BMDMs (PFA-fixed) located at the center of the TC-treated well at 20X magnification by bright field microscopy. (E) mRNA levels of SASP-associated genes normalized to ActB as determined by qPCR. (F) BrdU incorporation by BMDMs in absence or presence of TNFα, respectively with time. (G) BMDMs were infected for 4 hours with *Mtb* H37Rv at MOI=10, followed by removal of extracellular bacteria by extensive washing with warm media. Intramacrophage survival was determined by enumerating CFU at 2 days post-infection. The data are means ± SEM. Data is representative of two independent experiments done with n≥2. (p>0.05: ns, p<0.05: *, p<0.01: **, p<0.001: ***, p<0.0001: ****, one-way ANOVA with Tukey's (B, C, F, G) or two-way ANOVA with Sidak's (E) multiple comparisons test).

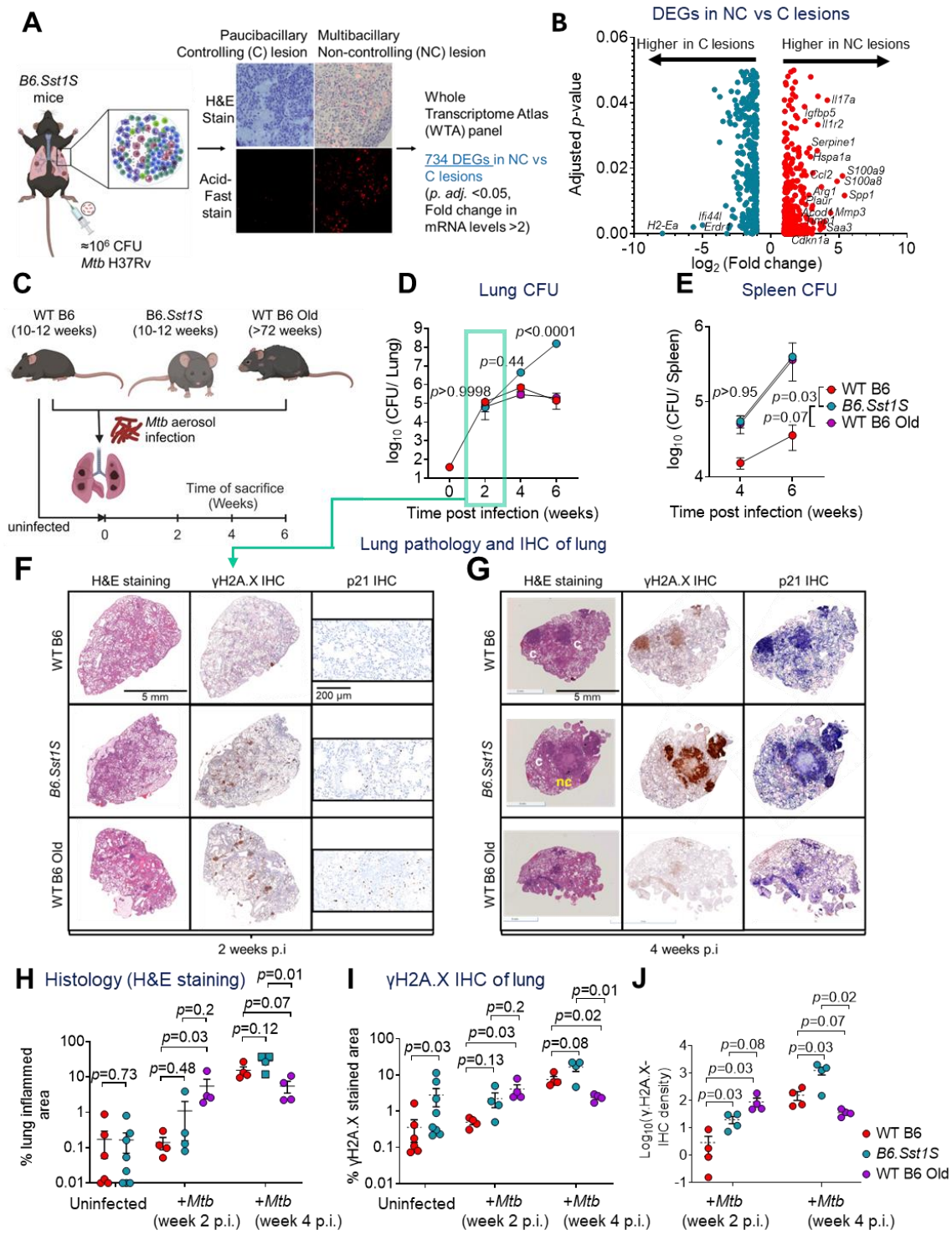

Figure 2. Detection of Senescence-associated markers during early stages of disease progression in *Mtb* infected mice. (A) Schematics of Spatial transcriptomics using a Nanostring GeoMX Digital Spatial Profiler to determine differential gene expression in cells at non-controlling multibacillary granulomatous lesions (*NC*) relative to controlling lesions (*C*) in *B6.Sst1S* mice lungs. (n= 8 ROI). (B) Volcano plot to show differentially expressed genes between controlling and non-controlling granulomatous lesions. Significantly upregulated (fold change> 2) and downregulated (fold change< 2) genes (*p.adj*< 0.05) in *NC* relative to *C*

granulomas are shown in red and cyan, respectively. Top senescence associated genes in upregulated DEGs are labelled. (C) Schematics of the experimental strategy to measure senescence markers *in vivo* at 2- and 4-weeks post infection. Day1 CFU=39. *Mtb* H37Rv burden at indicated time points in WT B6, *B6.Sst1S* and WT B6 old mice (D) lungs and (E) spleen. The data are means ± SEM. *p* was determined by two-way ANOVA with Tukey's multiple comparisons test ($p>0.05$: ns, $p<0.05$: *, $p<0.0001$: ****). Representative H&E-stained and Immunohistochemistry against γH2A.X and p21 of mice lungs at (F) 2 weeks p.i. (arrow indicates no difference in *Mtb* burden) and (G) 4 weeks p.i. (H) ImageJ quantification of lung pathology (H&E-stained area) in uninfected mice and *Mtb* H37Rv infected mice lungs at 2 weeks and 4 weeks p.i. (n=4-6). Squares indicate necrotic granulomas. (I) ImageJ quantification of γH2A.X-stained area in uninfected mice and *Mtb* H37Rv infected mice lungs, and (J) corresponding γH2A.X-IHC intensity at 2 weeks and 4 weeks p.i. (n=4-6 mice/group). The data are means ± SEM. Each data point represents a mouse. Statistical analysis between two groups was measured by unpaired two- tailed Student's t test (normal distribution) or Mann Whitney test.

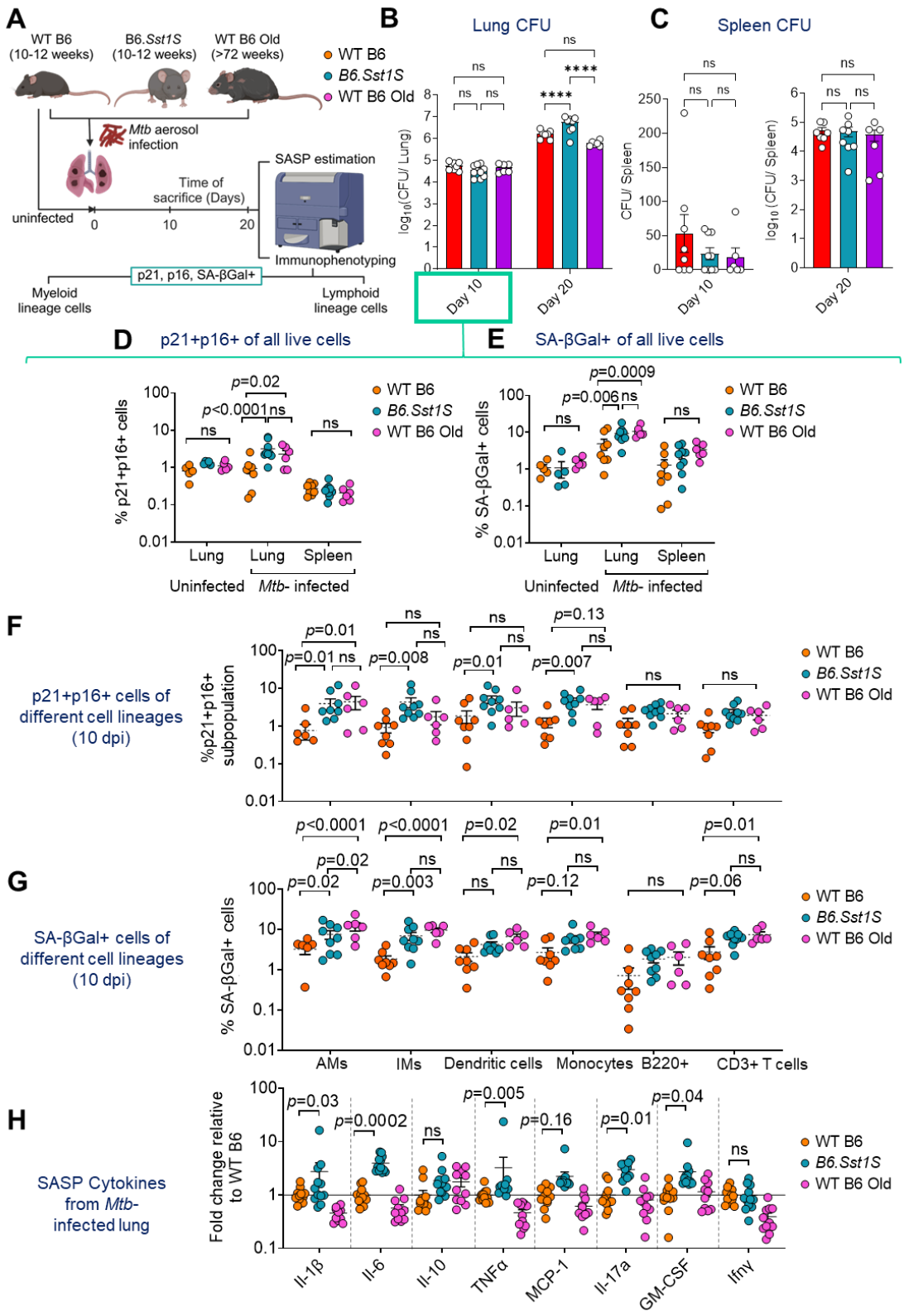

Figure 3. Detection of senescent cell population and SASP cytokines by flow cytometry during early stages of disease progression in *Mtb*-infected mice. (A) Schematics of the experimental strategy to measure senescence markers (p21, p16 and SA- βGal activity) and SASP cytokines levels in mice lungs

at 10 and 20 days p.i. Young WT B6, *B6.Sst1S*, and old WT B6 mice were aerosol-infected with 55 CFU of *Mtb* H37Rv. *Mtb* H37Rv burden in mice (B) lungs and (C) spleen are shown at indicated time points (n= 6-9 mice/ group). The data are means ± SEM. Each data point represents a mouse. Statistical analysis was calculated by two-way (B) or one- way (C) ANOVA with Tukey's multiple comparisons test. (p>0.05: ns, p<0.0001: ****). (D) %p21+p16+ and (E) %SA-βGal+ (CellEvent Senescence green+) cells out of all live lung (uninfected and *Mtb*-infected mice) and Spleen (*Mtb*-infected mice) cells at 10 days p.i. as determined by multicolor flow cytometry. (F) %p21+p16+ and (G) %SA-βGal+ cells out of different lung- cell types at 10 days p.i., as determined by multicolor flow cytometry. Gating for $p16^+$, $p21^+$, and SA-βGal^+ events for each cell type were established using Fluorescence minus one (FMO) controls and reference cells from *Mtb*-infected WT B6 mice (set at 1%). (AMs: Alveolar macrophages, IMs: Interstitial macrophages) **(H)** Normalized concentration of SASP- cytokines in lung homogenates at 20 dpi and 4 wpi relative to WT B6 mice as measured by a LEGENDplex™ Mouse Inflammation Panel. The data are means ± SEM. Each data point represents a mouse (n=11-12). (two-way ANOVA with Tukey's (D-G) or Dunnett's (H) multiple comparisons test).

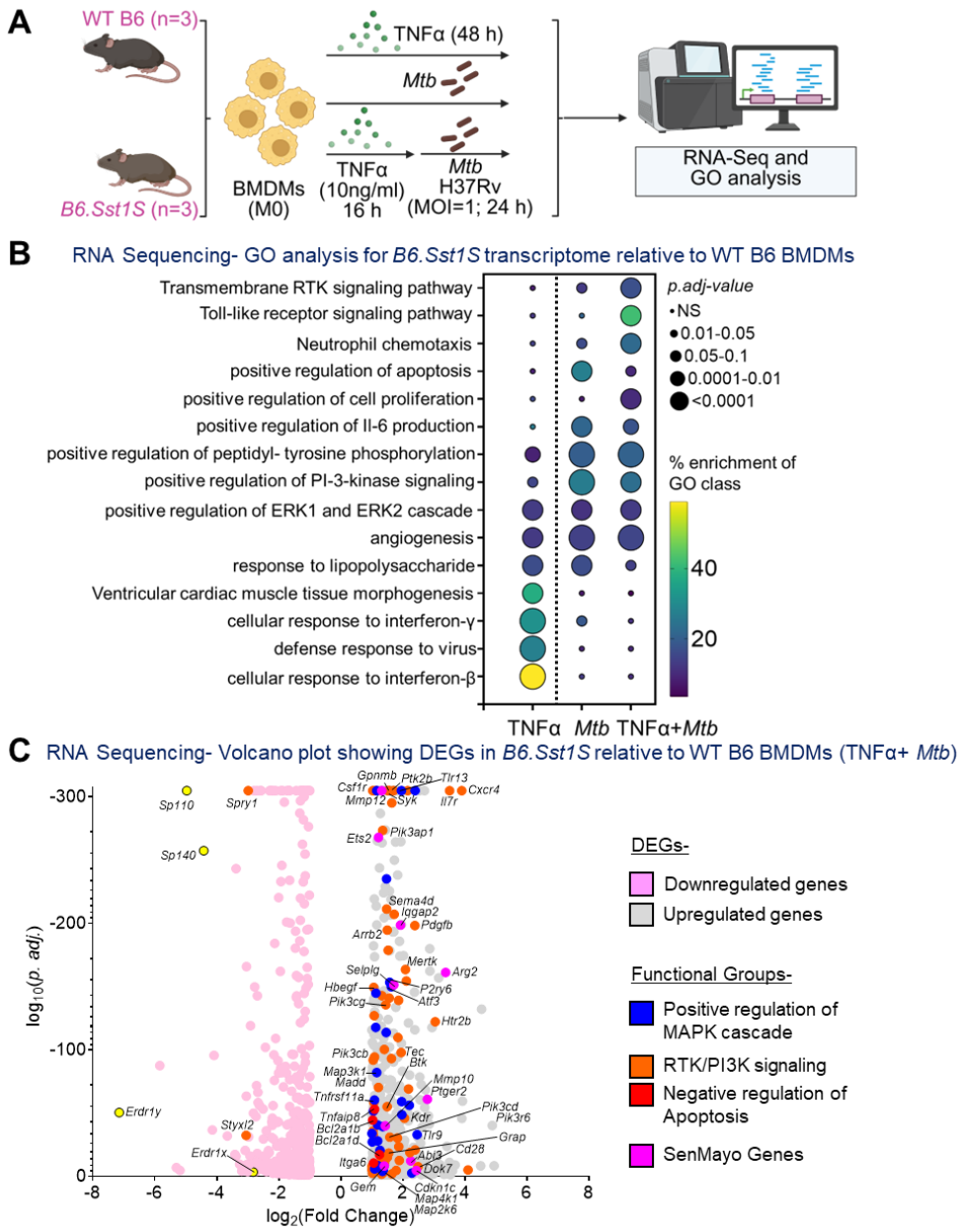

Figure 4. Global transcriptomics data by RNA Sequencing revealed upregulation of pro-survival pathways- PI3K-ERK1/2 and MAPK cascade in BMDMs derived from young *B6.Sst1S.* (A) Schematic of the experiment. (B) Selective representation of Gene-Ontology (GO) analysis for the differentially expressed genes indicating all enriched (*p.adj*< 0.05) signaling pathways under TNFα, *Mtb* and TNFα+ *Mtb*- treatment conditions. The size of the bubble indicates *p.adj* values relative to similarly treated WT B6, and color indicates the percentage of DEGs out of total genes in that GO class. (C) Volcano plot of DEGs (=1177) with upregulated genes in TNFα+ *Mtb- treated B6.Sst1S* BMDMs (log2 fold change >1; *p. adj.*< 0.05) shown in light gray and downregulated genes (log2 fold change <1; *p. adj.*< 0.05) shown in light pink, relative to stressed WT B6 BMDMs. Genes representative of top significantly enriched GO class- Receptor tyrosine kinase signaling/ PI3K pathway (shown in orange), MAPK cascade (blue), anti-apoptotic genes (red) and SenMayo gene set (pink) are shown. Top expected downregulated genes- Sp140, Sp110 and Erdr1 are shown in yellow.

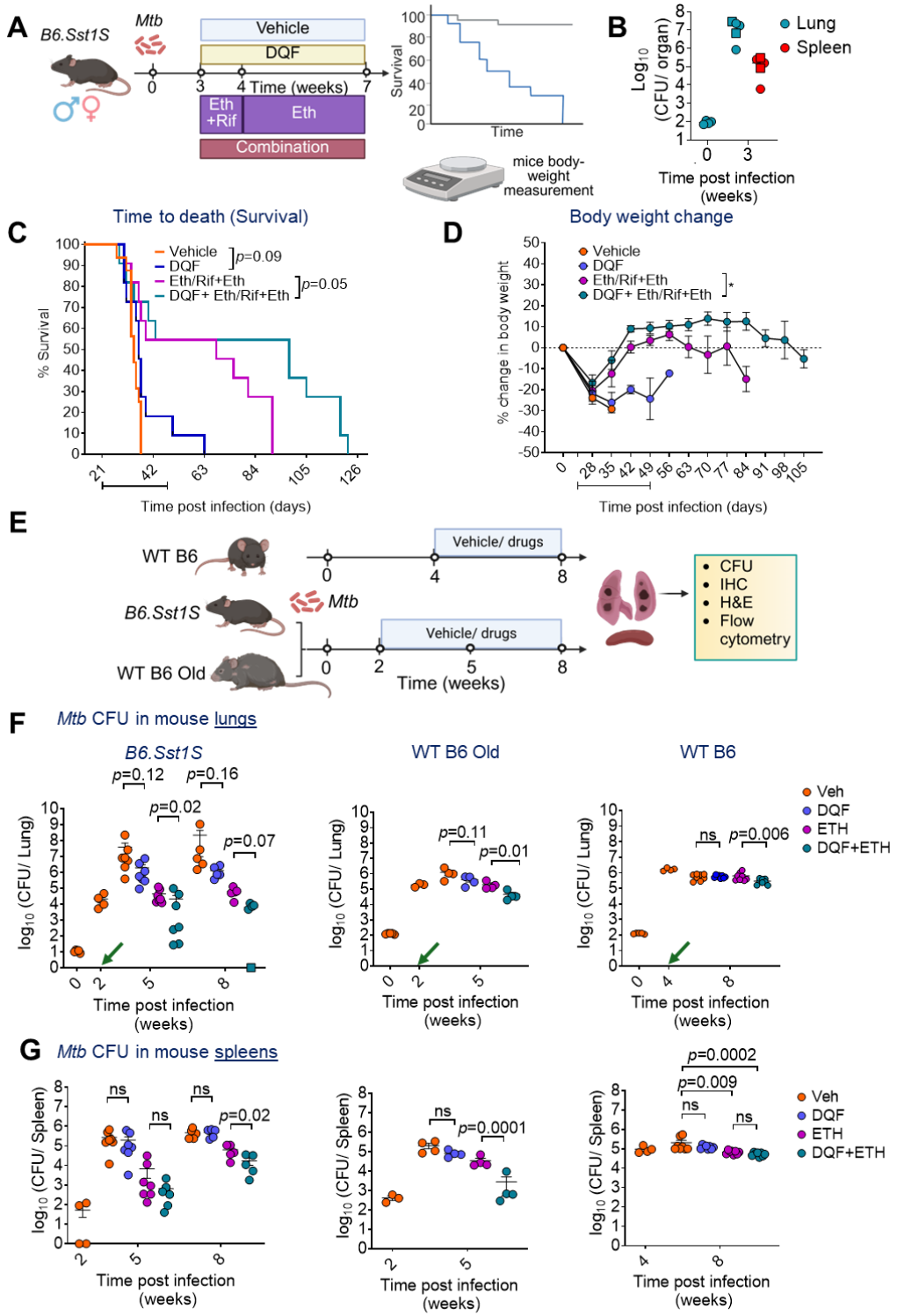

Figure 5. Senolytics DQF administration with or without anti-TB drug improved survival, body weight and reduced *Mtb* burden in mice. (A) Both male and female *B6.Sst1S* mice were aerosol infected with high-dose 91 CFU of *Mtb* H37Rv and at 3 weeks p.i., mice were oral gavaged with vehicle (n=16 mice)/ drugs (n=11 mice) for the next 4 weeks. (B) At 3 weeks p.i., the *Mtb* burden in lungs and spleen were $1.5*10^7$ and $1.6*10^5$ CFU, respectively. (circles indicate females and squares indicate males, n=4-5 mice).

1395 Mice were monitored for changes in body weight and survival after the start of drug treatment. (C) Kaplan-
1396 Meir survival curve of *B6.Sst1S* mice. Line indicates duration of therapy. Indicated *p* values are measured
1397 by log-rank (Mantel-Cox) test. (D) Changes in body weight are plotted as a % change in body weight of
1398 surviving mice relative to Day 1 p.i. over time. The data are means ± SEM. ($p<0.05$: *, two-way ANOVA
1399 with Tukey's multiple comparisons test). (E) The experimental strategy. Day 1 CFU in *B6.Sst1S* mice= 11
1400 (low dose); WT B6 young and old mice= 126. *Mtb* H37Rv burden in (F) lung and (G) spleen of WT B6,
1401 *B6.Sst1S* and old WT B6 mice at indicated time points (n=4-7). Square indicates CFU below the limit of
1402 detection (=10 CFU). The green arrow indicates the start of drug treatment. The data are means ± SEM.
1403 Each data point represents a mouse. n= 4-7 mice/ group. Statistical analysis was done by one-way ANOVA
1404 with Sidak's multiple comparison test or Kruskal-Wallis Dunn's multiple comparison test (5G-WT B6).

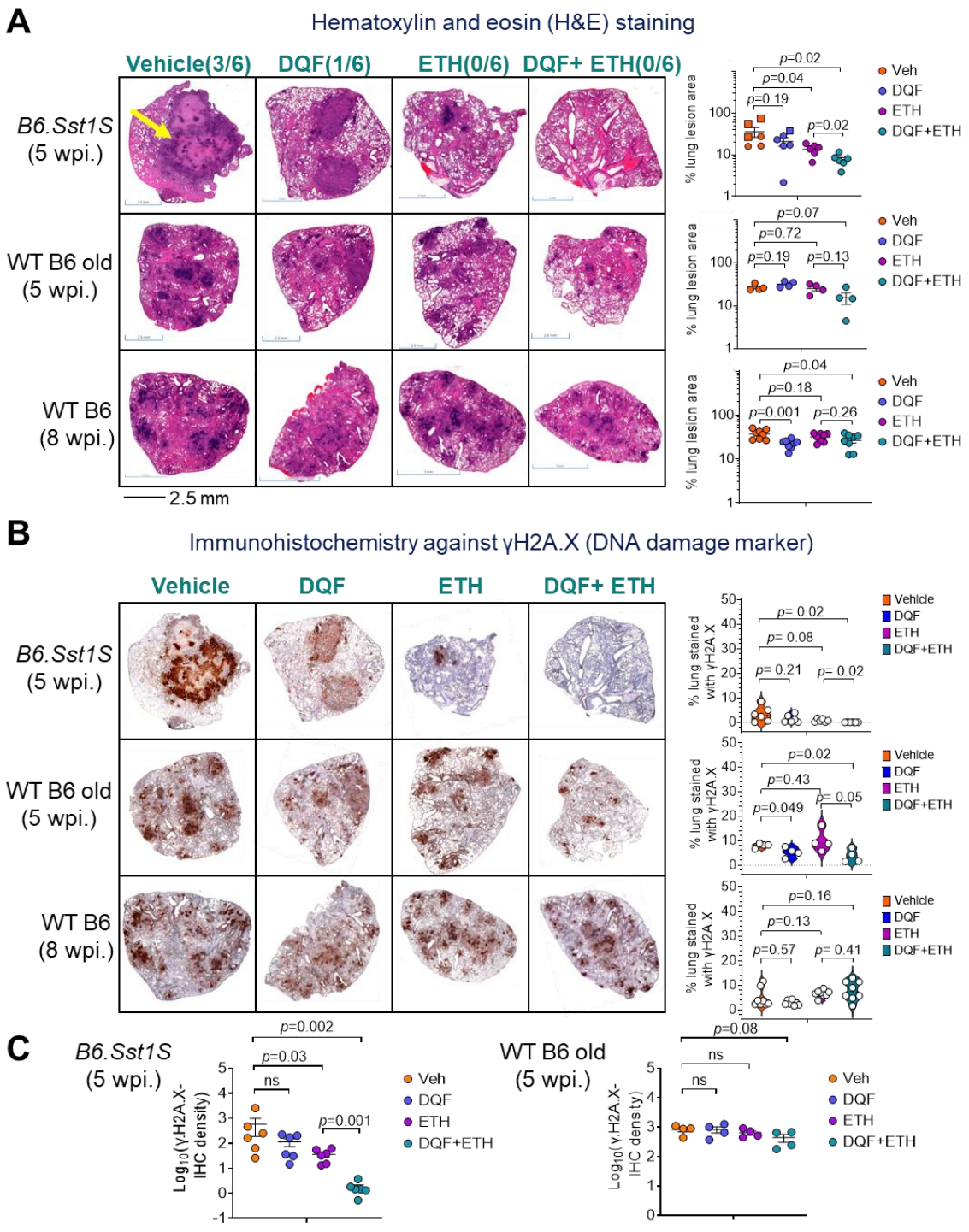

Figure 6. Senolytics administration alone, and in combination with Ethambutol reduced lung pathology and senescence- associated marker in *Mtb* H37Rv infected *B6.Sst1S* and WT B6 old mice. (A) Representative H&E-stained images of *Mtb*- infected mice lungs treated with Vehicle or drugs, and respective ImageJ- based quantification. Yellow arrow indicates necrotic granuloma in Vehicle treated *B6.Sst1S* mice at 5 wpi. The number in parenthesis indicate the number of mice with necrotic granuloma at 5 wpi. (B) Representative γH2A.X- Immunohistochemistry images of mice after lungs vehicle/ drugs treatment, and respective Violin plots to show ImageJ quantification of γH2A.X-stained area and (C)

1413 γH2A.X- stain intensity at indicated time points. Each data point represents a mouse. n=4-7 mice/group.
1414 Statistical analysis between two groups was done by unpaired two- tailed Student's t test or Mann-Whitney
1415 test.
1416
1417
1418
1419
1420
1421
1422
1423
1424
1425
1426
1427
1428
1429
1430
1431
1432
1433
1434
1435
1436
1437
1438
1439
1440

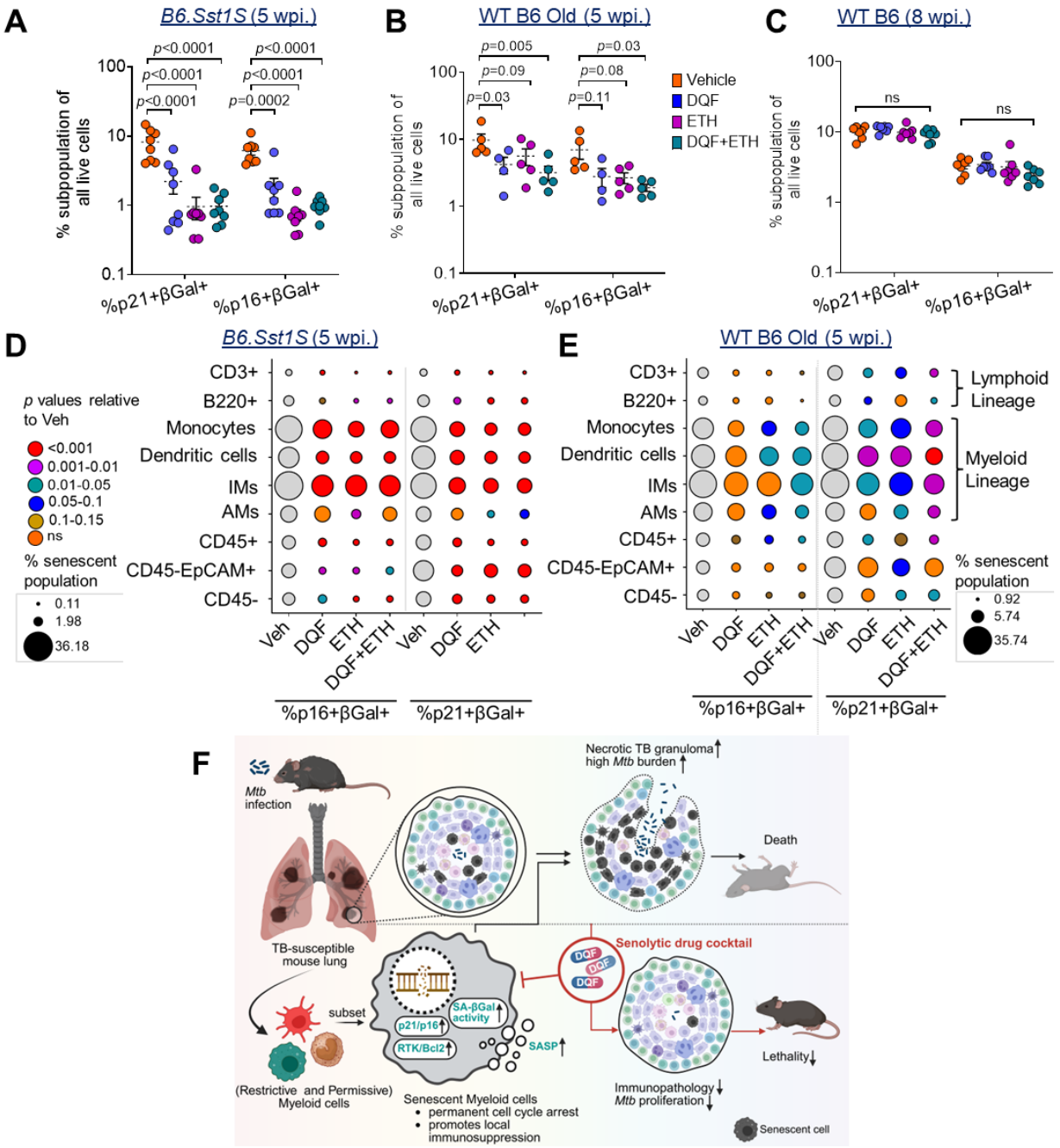

Figure 7. Senolytics administration alone, and in combination with Ethambutol reduced p21+SA-βGal+ or p16+SA-βGal+ senescent population in *Mtb* H37Rv infected *B6.Sst1S* and WT B6 old mice. %p21+βGal+ and %p16+βGal+ subpopulation observed in all live lung cells of Mtb- infected (A) *B6.Sst1S* (B) WT B6 old, and (C) young WT B6 mice (n= 5-8),. The data are means ± SEM. Each data point represents a mouse. Statistical analysis was calculated by two-way ANOVA with Dunnett's multiple comparisons test. Bubble plot to show %p21+βGal+ and %p16+βGal+ subpopulation in different lung cell types in *Mtb*-infected (D) *B6.Sst1S* mice (n= 8) and (E) WT B6 old mice (n= 5) at indicated timepoint and treatment groups. The size of the bubble indicates %subpopulation out of all of particular cell types and color is adjusted *p* values relative to the Veh group. Statistics are calculated by one-way ANOVA with Tukey's multiple comparisons test. (F) Proposed model showing the crosstalk between senescence and necrotic granuloma trajectory.